2012

Boost-Invariant (2+1)-Dimensional Anisotropic Hydrodynamics

Mauricio Martinez

Radoslaw Ryblewski

Michael T. Strickland
Gettysburg College

Martinez, Mauricio, Radoslaw Ryblewski, and Michael Strickland. "Boost-Invariant (2+1)-Dimensional Anisotropic Hydrodynamics." Physical Review C 85.6 (2012): 064913-1 – 064913-19.

Boost-Invariant (2+1)-Dimensional Anisotropic Hydrodynamics

Abstract
We present results of the application of the anisotropic hydrodynamics (aHydro) framework to (2+1)-dimensional boost-invariant systems. The necessary aHydro dynamical equations are derived by taking moments of the Boltzmann equation using a momentum-space anisotropic one-particle distribution function. We present a derivation of the necessary equations and then proceed to numerical solutions of the resulting partial differential equations using both realistic smooth Glauber initial conditions and fluctuating Monte Carlo Glauber initial conditions. For this purpose we have developed two numerical implementations: one that is based on straightforward integration of the resulting partial differential equations supplemented by a two-dimensional weighted Lax-Friedrichs smoothing in the case of fluctuating initial conditions and another that is based on the application of the Kurganov-Tadmor central scheme. For our final results we compute the collective flow of the matter via the laboratory-frame energy-momentum tensor eccentricity as a function of the assumed shear viscosity-to-entropy ratio, proper time, and impact parameter.

Keywords
anisotropic hydrodynamics framework, aHydro, boost-invariant systems

Disciplines
Nuclear | Physics

Boost-invariant (2 + 1)-dimensional anisotropic hydrodynamics

Mauricio Martinez,[1] Radoslaw Ryblewski,[2] and Michael Strickland[3,4]

[1]*Departamento de Física de Partículas, Universidade de Santiago de Compostela, Santiago de Compostela, E-15782 Galicia, Spain*

[2]*The H. Niewodniczański Institute of Nuclear Physics, Polish Academy of Sciences, PL-31342 Kraków, Poland*

[3]*Physics Department, Gettysburg College, Gettysburg, Pennsylvania 17325, USA*

[4]*Frankfurt Institute for Advanced Studies, D-60438 Frankfurt am Main, Germany*

(Received 13 April 2012; published 19 June 2012)

We present results of the application of the anisotropic hydrodynamics (aHydro) framework to (2 + 1)-dimensional boost-invariant systems. The necessary aHydro dynamical equations are derived by taking moments of the Boltzmann equation using a momentum-space anisotropic one-particle distribution function. We present a derivation of the necessary equations and then proceed to numerical solutions of the resulting partial differential equations using both realistic smooth Glauber initial conditions and fluctuating Monte Carlo Glauber initial conditions. For this purpose we have developed two numerical implementations: one that is based on straightforward integration of the resulting partial differential equations supplemented by a two-dimensional weighted Lax-Friedrichs smoothing in the case of fluctuating initial conditions and another that is based on the application of the Kurganov-Tadmor central scheme. For our final results we compute the collective flow of the matter via the laboratory-frame energy-momentum tensor eccentricity as a function of the assumed shear viscosity-to-entropy ratio, proper time, and impact parameter.

DOI: 10.1103/PhysRevC.85.064913 PACS number(s): 12.38.Mh, 24.10.Nz, 25.75.Ld, 47.75.+f

I. INTRODUCTION

The goal of ultrarelativistic heavy-ion collision experiments at the Relativistic Heavy Ion Collider at Brookhaven National Laboratory (RHIC) and the Large Hadron Collider (LHC) at CERN is to create a tiny volume of matter ($\sim$1000 fm^3) which has been heated to a temperature exceeding that necessary to create a quark-gluon plasma. It was shown early that ideal relativistic hydrodynamics is able to reproduce the soft collective flow of the matter and single-particle spectra produced at RHIC [1–4]. Based on this, there was a concerted effort to develop a more systematic framework for describing the soft collective motion. This effort resulted in a number of works dedicated to the development and application of relativistic viscous hydrodynamics to relativistic heavy-ion collisions [5–26].

One of the weakness of the traditional viscous hydrodynamics approach is that it relies on an implicit assumption that the system is close to thermal equilibrium which implies that the system is also very close to being isotropic in momentum space. However, one finds during the application of these methods to relativistic heavy-ion collisions that this assumption breaks down at the earliest times after the initial impact of the two nuclei due to large momentum-space anisotropies in the p_T-p_L plane which can persist for many fm/c [27]. In addition, one finds that near the transverse and longitudinal edges of the system these momentum-space anisotropies are large at all times [27–31]. Similar conclusions have been obtained in the context of strongly coupled systems where it has been shown using the anti-de Sitter space/conformal field theory correspondence one achieves viscous hydrodynamical behavior at times when the system still possesses large momentum-space anisotropies and that these anisotropies remain large throughout the evolution [32–38]. Based on these results, one is motivated to obtain a dynamical framework that can accommodate potentially large momentum-space anisotropies.

In this paper we follow up recent work which aims to extend the applicability of space-time evolution models for the bulk dynamics of a quark-gluon plasma to situations in which there can be large momentum-space anisotropies. Initial studies along this direction focused on boost-invariant expansion in systems which were transversally homogeneous [39,40]. The motivation and conceptual setup of Refs. [39,40] were similar in the sense that they both relaxed the assumption of the system being nearly isotropic in momentum space; however, there was a key conceptual difference in the derivation of the resulting dynamical equations. In Ref. [39] an entropy source was postulated which satisfied the minimal constraints necessary in the limit of small momentum-space anisotropy and then the authors assumed a constant rate of isotropization regardless of the local typical momentum of the plasma constituents. In Ref. [40] the equations of motion were derived by taking moments of the Boltzmann equation and supplemented by a requirement that, in the limit of small momentum-space anisotropy, these equations reproduced those of second-order Israel-Stewart viscous hydrodynamics [41–43]. The result of this matching was that the relaxation rate of the system was necessarily proportional to the local hard momentum scale.[1] This allowed the authors of Ref. [40] to smoothly match onto second-order viscous hydrodynamics when the system was nearly isotropic in momentum space.

The phenomenological consequence of these two different results for the relaxation rate is quite important. If the relaxation rate is proportional to the local hard momentum scale, then one expects a slower relaxation to isotropy when the local hard momentum scale is reduced. This occurs at late times

[1]In this context, the hard momentum scale corresponds to the typical average momentum scale of the particles of the system. When one has local isotropic thermal equilibrium, the average momentum scale corresponds to the temperature of the system.

in the one-dimensional case since the local hard momentum scale is dynamically lowered due to expansion. Even more importantly, having a relaxation rate which is proportional to the hard momentum scale has important consequences for the evolution of the matter near the longitudinal and transverse edges of the system where the local temperature is also initially lower. The first demonstration of this effect was in Ref. [28] which studied the one-dimensional non-boost-invariant evolution of a system which was transversally homogeneous. This work followed similar developments in Ref. [29] where a constant relaxation rate was assumed. A comparison of the results of these two papers shows that one sees much larger momentum-space anisotropies at large spatial rapidity being developed if one uses a relaxation rate which is proportional to the local hard momentum scale.

Since these works were published, the anisotropic hydrodynamics methodology has been extended to include boost-invariant transverse dynamics [44,45]; however, these papers once again assumed a fixed rate of relaxation to isotropy. In this paper we study the effect of using a more realistic relaxation rate which is proportional to the hard momentum scale [40], thereby allowing a smooth matching to second-order viscous hydrodynamics. We present a derivation of the necessary equations and then proceed to numerical solutions of the resulting partial differential equations using both realistic smooth Glauber initial conditions and fluctuating Monte Carlo Glauber initial conditions. For this purpose, we have developed two numerical implementations: one that is based on straightforward integration of the resulting partial differential equations supplemented by a two-dimensional weighted Lax-Friedrichs smoothing in the case of fluctuating initial conditions and another that is based on the application of the Kurganov-Tadmor central scheme. For our final results we compute the collective flow of the matter via the laboratory-frame energy-momentum tensor eccentricity as a function of the assumed shear viscosity-to-entropy ratio, proper time, and impact parameter. We also present results for the dependence of the momentum-space anisotropy in the full transverse plane and show that in regions where the temperature is low one can develop sizable momentum-space anisotropies. As a control test we compare with second-order viscous hydrodynamics in the limit of small shear viscosities and demonstrate that the anisotropic hydrodynamics (aHydro) framework is able to reproduce the temperature and flow profiles obtained from second-order viscous hydrodynamics in this limit.

The structure of the paper is as follows: In Sec. II we introduce the tensor basis we will use in the case that the system is anisotropic in momentum space and derive the partial differential equations necessary for the dynamical evolution by taking moments of the Boltzmann equation. In Sec. III we present the types of smooth initial conditions we will use. In Sec. IV we introduce the three numerical algorithms (centered differences, weighted LAX, and hybrid Kurganov-Tadmor) we will we use to solve the resulting partial differential equations. In Sec. V we compare with second-order viscous hydrodynamics for noncentral collisions and present our final results. In Sec. VI we present our conclusions and a future outlook. Finally, in three appendices we include a comparison of entropy production in second-order viscous hydrodynamics and aHydro, some numerical checks of convergence, etc., and a brief rederivation of the $0+1$D Bjorken model using our tensor formalism.

II. KINETIC THEORY APPROACH TO ANISOTROPIC HYDRODYNAMICS

In this section we describe our theoretical framework for describing relativistic plasmas which are anisotropic in momentum space. Our setup is based on the kinetic theory approach to nonequilibrium systems [41]. There are different methods for constructing approximate solutions of the relativistic Boltzmann equation [41]. The most well-known approach is due to Israel and Stewart [42,46]. In this approach, one expands the distribution function around a local thermal equilibrated distribution function, $f_{\rm eq}(x,\,p)$, in terms of a series of irreducible Lorentz tensors[2] of particle momentum p^μ

$$\begin{aligned} f(x,\,p) &= f_{\rm eq}(x,\,p)\,[1+\phi(x,\,t)], \\ &= f_{\rm eq}(x,\,p)\,[1+c(x,\,t)+c_\mu p^{\langle\mu\rangle}+c_{\mu\nu}p^{\langle\mu}p^{\nu\rangle} \\ &\quad +c_{\mu\nu\lambda}p^{\langle\mu}p^\nu p^{\lambda\rangle}+\cdots], \end{aligned} \tag{2.1}$$

where the angle brackets above stand for symmetrized tensors which are orthogonal to the fluid four-velocity u^μ [26,41]. The thermal equilibrium distribution function has the functional form

$$f_{\rm eq}=\left\{\exp\left[\frac{p^\mu u_\mu(x)-\mu(x)}{T(x)}\right]+a\right\}^{-1}, \tag{2.2}$$

where $a=\pm1$ gives Fermi-Dirac or Bose-Einstein statistics and $a=0$ gives Maxwell-Boltzmann statistics.

The distribution function (2.1) is usually expanded until second order, i.e., just keeping the terms 1, $p^{\langle\mu\rangle}$, and $p^{\langle\mu}p^{\nu\rangle}$. An important aspect in the construction of irreducible tensor basis is the decomposition of the four-momentum p^μ of a particle in Minkowski space. One assumes the existence of a timelike normalized vector field $u^\mu(x)$ (which is identified with the fluid velocity) and an operator $\Delta_{\mu\nu}$ which is symmetric, traceless, and orthogonal to $u^\mu(x)$ such that $p^\mu=Eu^\mu+\Delta^{\mu\nu}p_\nu$ [26,41]. This decomposition allows one to have an irreducible nth-rank tensor basis which is complete and orthogonal [26,41].

An alternative but equivalent treatment for expanding the distribution function in terms of an irreducible nth-rank tensor basis was developed by Anderson [47]. This method instead decomposes the four-momentum p^μ of a particle as

$$p^\mu=Eu^\mu+\sum_{i=1}^{3}p_i x_i^\mu, \tag{2.3}$$

where u^μ is the fluid velocity and x_i^μ is a set of orthonormal vectors which are spacelike and orthogonal to u^μ. With this

[2]We point out that in the original approach by Israel and Stewart, the decomposition basis is not orthogonal and, therefore, the exact form of the transport coefficients cannot be obtained once the expansion is truncated. Recently, Denicol *et al.* showed how to correct this and expand properly the distribution function in terms of a complete and orthogonal set of irreducible tensors of a particle with momentum p^μ [26].

decomposition one can also find a suitable irreducible tensor representation [47]. We will follow this decomposition closely since it is the most convenient vector basis for a system which is anisotropic in momentum space along some preferred direction(s).

In the rest of this section, we use the vector basis decomposition (2.3) to construct second-rank tensors. As a particular case, we construct the energy-momentum tensor for a (2 + 1)-dimensional boost-invariant anisotropic plasma and derive the dynamical equations of motion by taking moments of the Boltzmann equation. Our discussion is restricted to the case of vanishing chemical potential.

A. Vector basis

In this paper we will concentrate on systems which possess a preferred direction associated with a single direction in momentum space. It is possible to construct a tensor basis which allows for multiple anisotropy directions; however, we restrict our considerations to this simpler case since taking into account the momentum-space anisotropy along the beamline direction is of particular importance for heavy-ion phenomenology. To begin, we will specify a tensor basis which is completely general and not subject to any symmetry constraints and then add the necessary symmetry constraints when needed.

A general tensor basis can be constructed by introducing 4 four-vectors which in the local rest frame (LRF) are

$$\begin{aligned} X^\mu_{0,\mathrm{LRF}} &\equiv u^\mu_{\mathrm{LRF}} = (1,0,0,0),\\ X^\mu_{1,\mathrm{LRF}} &\equiv x^\mu_{\mathrm{LRF}} = (0,1,0,0),\\ X^\mu_{2,\mathrm{LRF}} &\equiv y^\mu_{\mathrm{LRF}} = (0,0,1,0),\\ X^\mu_{3,\mathrm{LRF}} &\equiv z^\mu_{\mathrm{LRF}} = (0,0,0,1). \end{aligned} \tag{2.4}$$

These four-vectors are orthonormal in all frames. The vector X^μ_0 is associated with the four-velocity of the local rest frame and is conventionally called u^μ and one can also identify $X^\mu_1 = x^\mu$, $X^\mu_2 = y^\mu$, and $X^\mu_3 = z^\mu$ as indicated above. We will use the two different labels for these vectors interchangeably depending on convenience since the notation with numerical indices allows for more compact expressions in many cases. Note that, in the laboratory frame, the three spacelike vectors X^μ_i can be written entirely in terms of $X^\mu_0 = u^\mu$. This is because X^μ_i can be obtained by a sequence of Lorentz transformations/rotations applied to the local rest frame expressions specified above. We will return to this issue and construct explicit laboratory-frame representations of these four-vectors later.

Finally, we point out that one can express the metric tensor itself in terms of these four-vectors as

$$g^{\mu\nu} = X^\mu_0 X^\nu_0 - \sum_{i=1}^{3} X^\mu_i X^\nu_i. \tag{2.5}$$

In addition, the standard transverse projection operator which is orthogonal to X^μ_0 can be rewritten in terms of the vector basis (2.4) as

$$\Delta^{\mu\nu} = g^{\mu\nu} - X^\mu_0 X^\nu_0 = -\sum_{i=1}^{3} X^\mu_i X^\nu_i \tag{2.6}$$

such that $u_\mu \Delta^{\mu\nu} = u_\nu \Delta^{\mu\nu} = 0$. We note that the spacelike components of the tensor basis are eigenfunctions of this operator, i.e., $X_{i\mu}\Delta^{\mu\nu} = X^\nu_i$.

B. Second-rank tensors

A general rank 2 tensor can be decomposed using the four-vectors X^μ_α. In general, there are 16 possible terms,

$$\begin{aligned} A^{\mu\nu}(t,\mathbf{x}) &= \sum_{\alpha,\beta=0}^{3} c_{\alpha\beta} X^\mu_\alpha X^\nu_\beta,\\ &= c_{00} X^\mu_0 X^\nu_0 + \sum_{i=1}^{3} c_{ii} X^\mu_i X^\nu_i + \sum_{\substack{\alpha,\beta=0\\ \alpha\neq\beta}}^{3} c_{\alpha\beta} X^\mu_\alpha X^\nu_\beta,\\ &= c_{00} g^{\mu\nu} + \sum_{i=1}^{3} \underbrace{(c_{ii} + c_{00})}_{\equiv d_{ii}} X^\mu_i X^\nu_i + \sum_{\substack{\alpha,\beta=0\\ \alpha\neq\beta}}^{3} c_{\alpha\beta} X^\mu_\alpha X^\nu_\beta, \end{aligned} \tag{2.7}$$

where it is understood that the coefficients $c_{\alpha\beta}$ now contain all of the space-time dependence.

C. Second-rank symmetric tensors

If a two tensor is symmetric under the interchange of μ and ν, then $c_{\alpha\beta} = c_{\beta\alpha}$ and we can write

$$\begin{aligned} A^{\mu\nu}(t,\mathbf{x}) &= c_{00} g^{\mu\nu} + \sum_{i=1}^{3} d_{ii} X^\mu_i X^\nu_i\\ &\quad + \sum_{\substack{\alpha,\beta=0\\ \alpha>\beta}}^{3} c_{\alpha\beta}\left(X^\mu_\alpha X^\nu_\beta + X^\mu_\beta X^\nu_\alpha\right) \end{aligned} \tag{2.8}$$

and there are only then 10 independent terms.

1. *Energy-momentum tensor for ideal hydrodynamics*

Since the energy-momentum tensor is a symmetric tensor of second rank, Eq. (2.8) can be used

$$\begin{aligned} T^{\mu\nu}(t,\mathbf{x}) &= t_{00} g^{\mu\nu} + \sum_{i=1}^{3} t_{ii} X^\mu_i X^\nu_i\\ &\quad + \sum_{\substack{\alpha,\beta=0\\ \alpha>\beta}}^{3} t_{\alpha\beta}\left(X^\mu_\alpha X^\nu_\beta + X^\mu_\beta X^\nu_\alpha\right), \end{aligned} \tag{2.9}$$

where we have relabeled the coefficients for this purpose. In the local rest frame we can identify the basis vectors via (2.4) and we have that $T^{00}_{\mathrm{LRF}} = \mathcal{E}$ and $T^{ii}_{\mathrm{LRF}} = \mathcal{P}_i$, where $\mathcal{E}$ is the energy density and $\mathcal{P}_i$ is the pressure in the i direction and all other components vanish. If the system is locally isotropic as is the case for ideal hydrodynamics, then $\mathcal{P}_i \equiv \mathcal{P}$. From Eq. (2.9) we have $T^{00}_{\mathrm{LRF}} = \mathcal{E} = t_{00}$ and $T^{ii}_{\mathrm{LRF}} = \mathcal{P} = -t_{00} + t_{ii}$ and since all off-diagonal components vanish we have $t_{\alpha\beta} = 0$

for all $\alpha \neq \beta$. This allows us to write

$$\begin{aligned} T^{\mu\nu}(t,\mathbf{x}) &= \mathcal{E}g^{\mu\nu} + (\mathcal{P}+\mathcal{E})\sum_{i=1}^{3} X_i^\mu X_i^\nu, \\ &= \mathcal{E}g^{\mu\nu} + (\mathcal{P}+\mathcal{E})\big(X_0^\mu X_0^\nu - g^{\mu\nu}\big), \\ &= (\mathcal{E}+\mathcal{P})X_0^\mu X_0^\nu - \mathcal{P}g^{\mu\nu}, \end{aligned} \tag{2.10}$$

where in going from the first to second line we have used Eq. (2.5). Using the conventional notation that $X_0^\mu = u^\mu$ we obtain

$$T^{\mu\nu} = (\mathcal{E}+\mathcal{P})u^\mu u^\nu - \mathcal{P}g^{\mu\nu}, \tag{2.11}$$

in agreement with the expected result. For later use we also note that

$$T^\mu{}_\mu \equiv \mathcal{T} = \mathcal{E} - 3\mathcal{P}. \tag{2.12}$$

2. Energy-momentum tensor for azimuthally symmetric anisotropic hydrodynamics

In the bulk of this paper we will consider systems for which the momentum-space particle distribution is azimuthally symmetric while the rotational symmetry in the $p_\perp$-p_L plane is broken. From here onward we will refer to this as *azimuthally symmetric*, which implies an assumed symmetry only in momentum-space and not in configuration space. In the case of azimuthally symmetric anisotropic hydrodynamics we have

$$\begin{aligned} T^{00}_{\rm LRF} &= \mathcal{E} = t_{00}, \quad T^{xx}_{\rm LRF} = \mathcal{P}_\perp = -t_{00} + t_{11}, \\ T^{yy}_{\rm LRF} &= \mathcal{P}_\perp = -t_{00} + t_{22}, \quad T^{zz}_{\rm LRF} = \mathcal{P}_L = -t_{00} + t_{33}, \end{aligned} \tag{2.13}$$

and, due to the azimuthal symmetry in momentum space, we must have $t_{11} = t_{22}$ which gives four equations for our four unknowns. Solving for the coefficients t one obtains

$$\begin{aligned} &T^{\mu\nu}(t,\mathbf{x}) \\ &= \mathcal{E}g^{\mu\nu} + (\mathcal{P}_\perp+\mathcal{E})\sum_{i=1}^{2} X_i^\mu X_i^\nu + (\mathcal{P}_L+\mathcal{E})X_3^\mu X_3^\nu, \\ &= \mathcal{E}g^{\mu\nu} + (\mathcal{P}_\perp+\mathcal{E})\sum_{i=1}^{3} X_i^\mu X_i^\nu + (\mathcal{P}_L-P_\perp)X_3^\mu X_3^\nu, \\ &= \mathcal{E}g^{\mu\nu} + (\mathcal{P}_\perp+\mathcal{E})\big(X_0^\mu X_0^\nu - g^{\mu\nu}\big) + (\mathcal{P}_L-P_\perp)X_3^\mu X_3^\nu, \\ &= (\mathcal{E}+\mathcal{P}_\perp)X_0^\mu X_0^\nu - \mathcal{P}_\perp g^{\mu\nu} + (\mathcal{P}_L-P_\perp)X_3^\mu X_3^\nu. \end{aligned} \tag{2.14}$$

Relabeling $X_0^\mu = u^\mu$ and $X_3^\mu = z^\mu$ to agree more closely with the notation of Ref. [45], we obtain

$$T^{\mu\nu} = (\mathcal{E}+\mathcal{P}_\perp)u^\mu u^\nu - \mathcal{P}_\perp g^{\mu\nu} + (\mathcal{P}_L-\mathcal{P}_\perp)z^\mu z^\nu, \tag{2.15}$$

which in the limit that $\mathcal{P}_\perp = \mathcal{P}_L \equiv \mathcal{P}$ reduces to Eq. (2.11). We again note for later use that

$$T^\mu{}_\mu \equiv \mathcal{T} = \mathcal{E} - 2\mathcal{P}_\perp - \mathcal{P}_L. \tag{2.16}$$

D. Explicit forms of the basis vectors

In the laboratory frame the three spacelike vectors X_i^μ can be written entirely in terms of $X_0^\mu = u^\mu$. This is because X_i^μ can be obtained by a sequence of Lorentz transformations/rotations applied to the local rest frame expressions specified above. To go from the laboratory frame to LRF we can apply a boost along the z axis followed by a rotation around the z axis and finally a boost along the x axis, i.e., $u_{\rm LRF} = L_x(\psi)R_z(\theta)L_z(\vartheta)u$ [48]. This specific transformation is chosen in order to ensure that the four-vector z^μ has no transverse components in all frames. To find the necessary vectors in the laboratory frame based on the LRF expressions (2.4) we apply the inverse operation $X^\mu_{\alpha,\rm LAB} = (L_x R_z L_z)^{-1} X^\mu_{\alpha,\rm LRF} = (L_z)^{-1}(R_z)^{-1}(L_x)^{-1} X^\mu_{\alpha,\rm LRF}$, which is explicitly given by

$$\begin{aligned} &X^\mu_{\alpha,\rm LAB} \\ &= \underbrace{\begin{pmatrix} \cosh\vartheta & 0 & 0 & \sinh\vartheta \\ 0 & 1 & 0 & 0 \\ 0 & 0 & 1 & 0 \\ \sinh\vartheta & 0 & 0 & \cosh\vartheta \end{pmatrix}}_{(L_z)^{-1}} \underbrace{\begin{pmatrix} 1 & 0 & 0 & 0 \\ 0 & \cos\phi & -\sin\phi & 0 \\ 0 & \sin\phi & \cos\phi & 0 \\ 0 & 0 & 0 & 1 \end{pmatrix}}_{(R_z)^{-1}} \\ &\times \underbrace{\begin{pmatrix} \cosh\psi & \sinh\psi & 0 & 0 \\ \sinh\psi & \cosh\psi & 0 & 0 \\ 0 & 0 & 1 & 0 \\ 0 & 0 & 0 & 1 \end{pmatrix}}_{(L_x)^{-1}} X^\mu_{\alpha,\rm LRF}, \end{aligned} \tag{2.17}$$

which gives

$$\begin{aligned} u^0 &= \cosh\psi\cosh\vartheta, \quad x^0 = \sinh\psi\cosh\vartheta, \\ u^1 &= \sinh\psi\cos\phi, \quad x^1 = \cosh\psi\cos\phi, \\ u^2 &= \sinh\psi\sin\phi, \quad x^2 = \cosh\psi\sin\phi, \\ u^3 &= \cosh\psi\sinh\vartheta, \quad x^3 = \sinh\psi\sinh\vartheta, \\ y^0 &= 0, \quad z^0 = \sinh\vartheta, \\ y^1 &= -\sin\phi, \quad z^1 = 0, \\ y^2 &= \cos\phi, \quad z^2 = 0, \\ y^3 &= 0, \quad z^3 = \cosh\vartheta. \end{aligned} \tag{2.18}$$

In the limit that the system is boost invariant one can identify $\vartheta = \varsigma$, where ς is the spatial rapidity defined through

$$t = \tau\cosh\varsigma, \quad z = \tau\sinh\varsigma, \tag{2.19}$$

where $\tau = \sqrt{t^2 - z^2}$ is the proper time. In the remainder of the paper, when we refer to a boost-invariant system we will use τ and ς as the longitudinal coordinates.

E. Dynamical equations

In this section, we derive the dynamical equations of motion by taking moments of the Boltzmann equation [41]

$$p^\mu \partial_\mu f(x,p) = -C[f]. \tag{2.20}$$

The moments are defined by multiplying the left- and right-hand sides of the Boltzmann equation by various powers of the four-momentum and then averaging in momentum space. This can be achieved via the $n^{\rm th}$ moment integral operator

$$\hat{\mathcal{I}}_n \equiv \int d\chi\; p^{\mu_1} p^{\mu_2} \cdots p^{\mu_n}, \tag{2.21}$$

where $n \geqslant 0$ is an integer and

$$\int d\chi \equiv \int \frac{d^4\mathbf{p}}{(2\pi)^3}\,\delta(p_\mu p^\mu - m^2)\,2\theta(p^0) = \int \frac{d^3\mathbf{p}}{(2\pi)^3}\,\frac{1}{p^0}. \tag{2.22}$$

F. Zeroth moment of the Boltzmann equation

The zeroth moment of the Boltzmann equation results from applying $\hat{\mathcal{I}}_0$ to both sides of Eq. (2.20)

$$\int d\chi\; p^\mu \partial_\mu f = J_0, \quad \partial_\mu \int \frac{d^3\mathbf{p}}{(2\pi)^3}\,\frac{p^\mu}{p^0}\, f = J_0, \quad \partial_\mu j^\mu = J_0, \tag{2.23}$$

where $J_n \equiv -\hat{\mathcal{I}}_n C[f]$. Note that we can rewrite the left-hand side of the last expression as $j^\mu = n u^\mu$, where n is the particle number density in the local rest frame. Expanding, we find

$$\partial_\mu j^\mu = Dn + n\theta, \tag{2.24}$$

where

$$D \equiv u^\mu \partial_\mu, \quad \theta \equiv \partial_\mu u^\mu, \tag{2.25}$$

allowing us to write a general expression for the zeroth moment of the Boltzmann equation

$$Dn + n\theta = J_0. \tag{2.26}$$

G. First moment of the Boltzmann equation

The first moment of the Boltzmann equation is equivalent to the requirement of energy and momentum conservation [41]

$$\partial_\mu T^{\mu\nu} = 0, \tag{2.27}$$

where $T^{\mu\nu}$ is the energy momentum tensor. In the following we derive evolution equations under different assumptions about the degree of symmetry of $T^{\mu\nu}$.

1. Ideal hydrodynamics

To begin we use the general form of the energy-momentum tensor for an isotropic system given in Eq. (2.11) to obtain

$$\partial_\mu T^{\mu\nu} = u^\nu D(\mathcal{E} + \mathcal{P}) + u^\nu(\mathcal{E} + \mathcal{P})\theta + (\mathcal{E} + \mathcal{P})Du^\nu - \partial^\nu \mathcal{P}, \tag{2.28}$$

where D and θ are defined in Eq. (2.25).

Canonically one takes projections of $\partial_\mu T^{\mu\nu} = 0$ parallel and perpendicular to u^μ. The parallel projection is obtained via $u_\nu \partial_\mu T^{\mu\nu}$ which gives

$$\begin{aligned} u_\nu \partial_\mu T^{\mu\nu} &= D(\mathcal{E} + \mathcal{P}) + (\mathcal{E} + \mathcal{P})\theta \\ &\quad + (\mathcal{E} + \mathcal{P})u_\nu Du^\nu - D\mathcal{P} = 0 \\ &= D\mathcal{E} + (\mathcal{E} + \mathcal{P})\theta = 0, \end{aligned} \tag{2.29}$$

where we have used $u_\nu u^\nu = 1$ and $u_\nu Du^\nu = \frac{1}{2}D(u_\nu u^\nu) = 0$. This gives us our first equation for ideal hydrodynamics. For the transverse projection we use $\Delta^{\mu\nu}$ defined in Eq. (2.6) which satisfies $\Delta_{\alpha\nu}u^\nu = 0$. This gives

$$\Delta^\alpha{}_\nu \partial_\mu T^{\mu\nu} = (\mathcal{E} + \mathcal{P})\Delta^\alpha{}_\nu Du^\nu - \Delta^\alpha{}_\nu \partial^\nu \mathcal{P} = 0. \tag{2.30}$$

Using the explicit form for $\Delta^\alpha{}_\nu = g^\alpha{}_\nu - u^\alpha u_\nu$ one obtains $\Delta^\alpha{}_\nu Du^\nu = Du^\alpha$. We can additionally define

$$\nabla^\alpha \equiv \Delta^\alpha{}_\nu \partial^\nu = -\sum_{\beta=1}^{3} X^\alpha_\beta X_{\nu\beta}\partial^\nu, \tag{2.31}$$

which is the gradient in the spacelike directions. Putting this together with Eq. (2.29), one obtains the following two equations:

$$\begin{aligned} D\mathcal{E} + (\mathcal{E} + \mathcal{P})\theta &= 0, \\ (\mathcal{E} + \mathcal{P})Du^\alpha - \nabla^\alpha \mathcal{P} &= 0. \end{aligned} \tag{2.32}$$

In the second case, α should be a spacelike index such that we have four equations in total which should be supplemented by the equation of state which can be expressed in the form of a constraint on the trace of the energy momentum tensor $T^\mu{}_\mu = \mathcal{T} = \mathcal{E} - 3\mathcal{P}$.

2. Ideal boost-invariant dynamics with transverse expansion

In this section we briefly review what happens when the system is boost invariant and we allow for inhomogeneities and flow in the transverse direction. In this case we have from Eq. (2.18)

$$\begin{aligned} u^\mu = (&\cosh\psi\cosh\varsigma, \sinh\psi\cos\phi, \sinh\psi\sin\phi, \\ &\cosh\psi\sinh\varsigma). \end{aligned} \tag{2.33}$$

It is convenient at this point to relabel the components of u^μ as

$$u^\mu = (u_0\cosh\varsigma, u_x, u_y, u_0\sinh\varsigma), \tag{2.34}$$

where the constraint $u_0^2 = 1 + u_x^2 + u_y^2$ should be satisfied. Changing to proper time and spatial rapidity, we obtain $u_\tau = u_0$, $u_\varsigma = 0$, and we have

$$\begin{aligned} D &= u^\mu \partial_\mu = u_0\partial_\tau + \mathbf{u}_\perp \cdot \nabla_\perp, \\ \theta &= \partial_\mu u^\mu = \partial_\tau u_0 + \nabla_\perp \cdot \mathbf{u}_\perp + \frac{u_0}{\tau}. \end{aligned} \tag{2.35}$$

For the transverse gradient it is convenient to rewrite

$$\nabla^i = \Delta^i{}_\nu \partial^\nu = \left(g^i{}_\nu - u^i u_\nu\right)\partial^\nu = \partial^i - u^i D, \tag{2.36}$$

such that the second equation in Eq. (2.32) can be expanded into three equations,

$$\begin{aligned} (\mathcal{E} + \mathcal{P})Du_x + u_x D\mathcal{P} + \partial_x \mathcal{P} &= 0, \\ (\mathcal{E} + \mathcal{P})Du_y + u_y D\mathcal{P} + \partial_y \mathcal{P} &= 0, \\ (\mathcal{E} + \mathcal{P})Du_0 + u_0 D\mathcal{P} - \partial_\tau \mathcal{P} &= 0, \end{aligned} \tag{2.37}$$

which, together with

$$D\mathcal{E} + (\mathcal{E} + \mathcal{P})\theta = 0, \tag{2.38}$$

would seem to give four equations for our four unknowns ($\mathcal{E}$, $\mathcal{P}$, u_x, and u_y since $u_0^2 = 1 + u_x^2 + u_y^2$); however, on inspection one finds that Eqs. (2.37) are not independent since u_0 times the third equation is equal to u_x times the first plus u_y times the second. We, therefore, have a choice of which equations to use and one can pick two of the three equations from Eq. (2.37), e.g., the first two. The final equation is then provided canonically by the equation of state which specifies, e.g., the energy density as a function of the pressure.

H. Azimuthally symmetric anisotropic hydrodynamics

We now proceed to the derivation of the dynamical equation for azimuthally symmetric anisotropic hydrodynamics. We remind the reader "azimuthally symmetric" means that the momentum-space particle distribution is azimuthally symmetric while the rotational symmetry in the $p_\perp$-p_L plane is broken. To begin we use the general form of the energy-momentum tensor for an azimuthally symmetric anisotropic system given in Eq. (2.15) to obtain

$$\begin{aligned}\partial_\mu T^{\mu\nu} &= u^\nu D(\mathcal{E}+\mathcal{P}_\perp) + u^\nu(\mathcal{E}+\mathcal{P}_\perp)\theta \\ &\quad + (\mathcal{E}+\mathcal{P}_\perp)Du^\nu - \partial^\nu \mathcal{P}_\perp + z^\nu D_L(\mathcal{P}_L-\mathcal{P}_\perp) \\ &\quad + z^\nu(\mathcal{P}_L-\mathcal{P}_\perp)\theta_L + (\mathcal{P}_L-\mathcal{P}_\perp)D_L z^\nu = 0,\end{aligned} \tag{2.39}$$

where

$$D_L \equiv z^\mu \partial_\mu, \quad \theta_L \equiv \partial_\mu z^\mu. \tag{2.40}$$

As before, we take projections of $\partial_\mu T^{\mu\nu} = 0$ parallel and perpendicular to u^μ. The parallel projection is obtained via $u_\nu \partial_\mu T^{\mu\nu}$, which gives

$$u_\nu \partial_\mu T^{\mu\nu} = D\mathcal{E} + (\mathcal{E}+\mathcal{P}_\perp)\theta + (\mathcal{P}_L-\mathcal{P}_\perp)u_\nu D_L z^\nu = 0, \tag{2.41}$$

where we have used $u_\nu u^\nu = 1$, $u_\nu Du^\nu = \frac{1}{2}D(u_\nu u^\nu) = 0$, and $u_\nu z^\nu = 0$. This gives us our first equation for azimuthally symmetric anisotropic hydrodynamics.

For the transverse projection we use $\Delta^{\mu\nu}$ defined in Eq. (2.6) which satisfies $\Delta_{\alpha\nu}u^\nu = 0$ and $\Delta_{\alpha\nu}z^\nu = z^\alpha$. This gives

$$\begin{aligned}\Delta^\alpha{}_\nu \partial_\mu T^{\mu\nu} &= (\mathcal{E}+\mathcal{P}_\perp)Du^\alpha - \nabla^\alpha \mathcal{P}_\perp + z^\alpha D_L(\mathcal{P}_L-\mathcal{P}_\perp) \\ &\quad + z^\alpha(\mathcal{P}_L-\mathcal{P}_\perp)\theta_L + (\mathcal{P}_L-\mathcal{P}_\perp)D_L z^\alpha \\ &\quad - (\mathcal{P}_L-\mathcal{P}_\perp)u^\alpha u_\nu D_L z^\nu = 0\,.\end{aligned} \tag{2.42}$$

1. Boost-invariant dynamics with transverse expansion

In this case, we have $z^\tau = 0$ and $z^\eta = 1/\tau$ such that

$$D_L = z^\mu \partial_\mu = \frac{\partial_\varsigma}{\tau}, \quad \theta_L = \partial_\mu z^\mu = 0. \tag{2.43}$$

From the first line above we find $u_\nu D_L z^\nu = u_0/\tau$. This allows us to simplify the parallel projection to

$$D\mathcal{E} + (\mathcal{E}+\mathcal{P}_\perp)\theta + (\mathcal{P}_L-\mathcal{P}_\perp)\frac{u_0}{\tau} = 0. \tag{2.44}$$

The transverse projections can also be simplified to

$$\begin{aligned}&(\mathcal{E}+\mathcal{P}_\perp)Du^\alpha + u^\alpha D\mathcal{P}_\perp + \partial_\alpha \mathcal{P}_\perp \\ &\quad + (\mathcal{P}_L-\mathcal{P}_\perp)\left(\frac{\partial_\varsigma z^\alpha}{\tau} - \frac{u_0}{\tau}u^\alpha\right) = 0,\end{aligned} \tag{2.45}$$

from which we can then obtain three equations

$$\begin{aligned}(\mathcal{E}+\mathcal{P}_\perp)Du_x + u_x D\mathcal{P}_\perp + \partial_x \mathcal{P}_\perp + (\mathcal{P}_\perp-\mathcal{P}_L)\frac{u_0 u_x}{\tau} &= 0, \\ (\mathcal{E}+\mathcal{P}_\perp)Du_y + u_y D\mathcal{P}_\perp + \partial_y \mathcal{P}_\perp + (\mathcal{P}_\perp-\mathcal{P}_L)\frac{u_0 u_y}{\tau} &= 0, \\ (\mathcal{E}+\mathcal{P}_\perp)Du_0 + u_0 D\mathcal{P}_\perp - \partial_\tau \mathcal{P}_\perp + (\mathcal{P}_\perp-\mathcal{P}_L)\frac{u_\perp^2}{\tau} &= 0.\end{aligned} \tag{2.46}$$

As was the case with ideal hydrodynamics, we see that u_0 times the third equation is equal to u_x times the first plus u_y times the second so it is redundant. This leaves us with the following three equations:

$$\begin{aligned}D\mathcal{E} + (\mathcal{E}+\mathcal{P}_\perp)\theta + (\mathcal{P}_L-\mathcal{P}_\perp)\frac{u_0}{\tau} &= 0, \\ (\mathcal{E}+\mathcal{P}_\perp)Du_x + \partial_x \mathcal{P}_\perp + u_x D\mathcal{P}_\perp + (\mathcal{P}_\perp-\mathcal{P}_L)\frac{u_0 u_x}{\tau} &= 0, \\ (\mathcal{E}+\mathcal{P}_\perp)Du_y + \partial_y \mathcal{P}_\perp + u_y D\mathcal{P}_\perp + (\mathcal{P}_\perp-\mathcal{P}_L)\frac{u_0 u_y}{\tau} &= 0.\end{aligned} \tag{2.47}$$

I. Distribution function for azimuthally symmetric systems

We next consider the one-particle distribution function f in the local rest frame and show that in the case of a system that is locally azimuthally symmetric in momentum space that it suffices to introduce one anisotropy parameter ξ and a single scale Λ [49]. To begin, we consider the general form

$$f(t,\mathbf{x},\mathbf{p}) = f_{\rm iso}(\sqrt{\bar{p}_\mu \Xi^{\mu\nu}(t,\mathbf{x})\bar{p}_\nu}). \tag{2.48}$$

$\Xi^{\mu\nu}(t,\mathbf{x})$ is a symmetric tensor, $f_{\rm iso}$ is an arbitrary isotropic distribution function, and $\bar{p}^\mu \equiv p^\mu/\Lambda$, where $\Lambda(t,\mathbf{x})$ is a momentum scale that can depend on space and time (the so-called hard momentum scale). In the case where the system is in thermal equilibrium, then $f_{\rm iso}$ would be given by a Bose-Einstein or Fermi-Dirac distribution function. Note that the argument of the square root in $f_{\rm iso}$ should remain greater than or equal to zero in order for f to be a single-valued real function.

If $\Xi^{\mu\nu}$ is a symmetric tensor and is diagonal in the local rest frame, we have

$$\Xi^{\mu\nu} = c_{00}u^\mu u^\nu + \sum_{i=1}^{3} c_{ii} X_i^\mu X_i^\nu, \tag{2.49}$$

and if, additionally, the system is symmetric under $x \leftrightarrow y$, then $c_{11} = c_{22} \equiv c_{\perp\perp}$ and we have

$$\begin{aligned}\Xi^{\mu\nu} &= c_{00}u^\mu u^\nu + c_{\perp\perp}\sum_{i=1}^{2} X_i^\mu X_i^\nu + c_{33}X_3^\mu X_3^\nu, \\ &= c_{00}u^\mu u^\nu - c_{\perp\perp}\Delta^{\mu\nu} + (c_{33}-c_{\perp\perp})X_3^\mu X_3^\nu.\end{aligned} \tag{2.50}$$

Using our ability to redefine $\Lambda \to \sqrt{c_{00}}\Lambda$ in Eq. (2.48) we can rescale our coefficients. Defining $c_{\perp\perp}/c_{00} \equiv \Phi$ and $(c_{33}-c_{\perp\perp})/c_{00} \equiv \alpha$ we can write compactly

$$\Xi^{\mu\nu} = u^\mu u^\nu - \Phi\Delta^{\mu\nu} + \alpha z^\mu z^\nu. \tag{2.51}$$

Contracting with four-momenta on both sides we find

$$\begin{aligned}p_\mu \Xi^{\mu\nu} p_\nu &= p_0^2 + \Phi\mathbf{p}^2 + \alpha p_z^2, \\ &= m^2 + (1+\Phi)\mathbf{p}^2 + \alpha p_z^2,\end{aligned} \tag{2.52}$$

where we have used $p_0^2 = \mathbf{p}^2 + m^2$. If we have a system of massless particles then

$$p_\mu \Xi^{\mu\nu} p_\nu = (1+\Phi)p_\perp^2 + (1+\Phi+\alpha)p_z^2, \tag{2.53}$$

and, in this case, we can once again use our ability to rescale $\Lambda \to \sqrt{(1+\Phi)}\Lambda$ and defining

$1+\xi \equiv (1+\Phi+\alpha)/(1+\Phi)$ we obtain

$$p_\mu \Xi^{\mu\nu} p_\nu = p_\perp^2 + (1+\xi) p_z^2, \tag{2.54}$$

which has the form of the argument of the original one-dimensional Romatschke-Strickland (RS) distribution function [49].

J. Number density and energy-momentum tensor with the RS distribution function

Based on the results of the last section, the functional form of the RS distribution function for a locally azimuthally symmetric expanding anisotropic plasma is

$$f(\mathbf{x},\mathbf{p},\tau) = f_{\rm RS}(\mathbf{p},\xi,\Lambda) = f_{\rm iso}\Big(\sqrt{\big[\mathbf{p}_\perp^2 + (1+\xi)p_z^2\big]/\Lambda^2}\Big), \tag{2.55}$$

where it is understood that on the right-hand side ξ and Λ can depend on space and time. Using this distribution function the number density is given by Refs. [50,51]

$$n(\xi,\Lambda) = \int \frac{d^3\mathbf{p}}{(2\pi)^3} f_{\rm RS} = \frac{n_{\rm iso}(\Lambda)}{\sqrt{1+\xi}}. \tag{2.56}$$

where $n_{\rm iso}(\Lambda)$ is the number density one obtains in the isotropic limit.

One can also evaluate the energy-momentum tensor in the LRF,

$$T^{\mu\nu} = \int \frac{d^3\mathbf{p}}{(2\pi)^3} \frac{p^\mu p^\nu}{p_0} f(\tau,\mathbf{x},\mathbf{p}). \tag{2.57}$$

By using the RS form Eq. (2.55) one gets the explicit components of the energy-momentum tensor [51]

$$\mathcal{E}(\Lambda,\xi) = T^{\tau\tau} = \mathcal{R}(\xi)\,\mathcal{E}_{\rm iso}(\Lambda), \tag{2.58a}$$

$$\mathcal{P}_\perp(\Lambda,\xi) = \tfrac{1}{2}(T^{xx}+T^{yy}) = \mathcal{R}_\perp(\xi)\mathcal{P}_{\rm iso}(\Lambda), \tag{2.58b}$$

$$\mathcal{P}_L(\Lambda,\xi) = -T^{\varsigma}_{\varsigma} = \mathcal{R}_{\rm L}(\xi)\mathcal{P}_{\rm iso}(\Lambda), \tag{2.58c}$$

where $\mathcal{P}_{\rm iso}(\Lambda)$ and $\mathcal{E}_{\rm iso}(\Lambda)$ are the isotropic pressure and energy density, respectively, and

$$\mathcal{R}(\xi) \equiv \frac{1}{2}\left(\frac{1}{1+\xi} + \frac{\arctan\sqrt{\xi}}{\sqrt{\xi}}\right), \tag{2.59a}$$

$$\mathcal{R}_\perp(\xi) \equiv \frac{3}{2\xi}\left[\frac{1+(\xi^2-1)\mathcal{R}(\xi)}{\xi+1}\right], \tag{2.59b}$$

$$\mathcal{R}_L(\xi) \equiv \frac{3}{\xi}\left[\frac{(\xi+1)\mathcal{R}(\xi)-1}{\xi+1}\right]. \tag{2.59c}$$

The equation of state can be imposed as a relationship between $\mathcal{E}_{\rm iso}$ and $\mathcal{P}_{\rm iso}$. In what follows we will assume an ideal equation of state which is appropriate for a conformal massless gas, i.e., $\mathcal{E}_{\rm iso} = 3\mathcal{P}_{\rm iso}$.

K. Relaxation time approximation

As mentioned in previous sections the dynamical equations necessary can be obtained by taking moments of the Boltzmann equation $p^\mu \partial_\mu f = -C[f]$. Here we use the relaxation time approximation with relaxation rate Γ

$$\mathcal{C}[f_{\rm RS}] = p_\mu u^\mu\, \Gamma[f_{\rm RS}(\mathbf{p},\xi,\Lambda,\varsigma) - f_{\rm eq}(|\mathbf{p}|,T)], \tag{2.60}$$

where ς is the spatial rapidity and we fix Γ such that the second-order viscous hydrodynamical equations are reproduced in the one-dimensional transversally symmetric case [40]. This requires that

$$\Gamma \equiv \frac{2}{\tau_\pi}, \quad \tau_\pi \equiv \frac{5}{4}\frac{\eta}{\mathcal{P}}, \tag{2.61}$$

which for an ideal equation of state results in

$$\Gamma = \frac{2T(\tau)}{5\bar{\eta}} = \frac{2\mathcal{R}^{1/4}(\xi)\Lambda}{5\bar{\eta}}, \tag{2.62}$$

where $\bar{\eta} = \eta/\mathcal{S}$ with η being the shear viscosity and $\mathcal{S}$ being the entropy density. We note that one could perform a matching to second-order viscous hydrodynamics including transverse dynamics, but we have not attempted to do so. Instead we use the 1D matching above and in the results section we show that numerical results from viscous hydrodynamics codes which include transverse dynamics are reproduced for small $\bar{\eta}$. That said, we have no reason to expect that the linearized equations would not reproduce second-order viscous hydrodynamics; however, this remains to be proven.

L. Dynamical equations of motion

Based on the results of the previous sections, we can derive the explicit form of the dynamical equations of motion for a (2 + 1)-dimensional boost-invariant system.

1. Zeroth moment of the Boltzmann equation

For the RS form the 0th moment of the Boltzmann equation (2.26) is written as

$$\frac{1}{1+\xi} D\xi - 6D(\log\Lambda) - 2\theta = 2\Gamma[1-\mathcal{R}^{3/4}(\xi)\sqrt{1+\xi}], \tag{2.63}$$

where we used explicitly the functional form of particle density n (2.56) and the scattering kernel for relaxation time approximation (2.60).

2. First moment of the Boltzmann equation

Using the RS form one finds the following three equations by requiring energy-momentum conservation

$$\begin{aligned}
\mathcal{R}'(\xi)D\xi + 4\mathcal{R}(\xi)D(\log\Lambda) &= -\left[\mathcal{R}(\xi)+\frac{1}{3}\mathcal{R}_\perp(\xi)\right]\Delta_\perp - \left[\mathcal{R}(\xi)+\frac{1}{3}\mathcal{R}_L(\xi)\right]\frac{u_0}{\tau},\\
[3\mathcal{R}(\xi)+\mathcal{R}_\perp(\xi)]\,Du_\perp &= -u_\perp\left\{\mathcal{R}'_\perp(\xi)\tilde{D}\xi + 4\mathcal{R}_\perp(\xi)\tilde{D}(\log\Lambda) + \frac{u_0}{\tau}[\mathcal{R}_\perp(\xi)-\mathcal{R}_L(\xi)]\right\},\\
u_y^2\,[3\mathcal{R}(\xi)+\mathcal{R}_\perp(\xi)]\,D\left(\frac{u_x}{u_y}\right) &= \mathcal{R}'_\perp(\xi)D_\perp\xi + 4\mathcal{R}_\perp(\xi)D_\perp(\log\Lambda),
\end{aligned} \tag{2.64}$$

where

$$\Delta_\perp \equiv \partial_\tau u_0 + \nabla_\perp \cdot \mathbf{u}_\perp, \quad \tilde{D} \equiv u_0 \partial_\tau + \frac{u_0^2}{u_\perp^2} \mathbf{u}_\perp \cdot \nabla_\perp,$$
$$D_\perp \equiv \hat{\mathbf{z}} \cdot (\mathbf{u}_\perp \times \nabla_T) = u_x \partial_y - u_y \partial_x, \tag{2.65}$$

$\mathbf{u}_\perp \equiv (u_x, u_y)$, and $u_0^2 = 1 + u_\perp^2$.

III. INITIAL CONDITIONS

We consider collisions of symmetric nuclei, each containing A nucleons. We will study both participant and binary collision type initial conditions [52] using a Woods-Saxon distribution for each nuclei's transverse profile [53]. For an individual nucleus we take the density to be

$$n_A(r) = \frac{n_0}{1 + e^{(r-R)/d}}, \tag{3.1}$$

where $n_0 = 0.17\ \text{fm}^{-3}$ is the central nucleon density, $R = (1.12A^{1/3} - 0.86A^{-1/3})$ fm is the nuclear radius, and $d = 0.54$ fm is the "skin depth." The density is normalized such that $\lim_{A\to\infty} \int d^3r\, n_A(r) = A$, where A is the total number of nucleons in the nucleus. The normalization condition fixes n_0 to the value specified above. From the nucleon density we, first, construct the thickness function in the standard way by integrating over the longitudinal direction, i.e.,

$$T_A(x, y) = \int_{-\infty}^{\infty} dz\, n_A(\sqrt{x^2 + y^2 + z^2}). \tag{3.2}$$

With this in hand we can construct the overlap density between two nuclei whose centers are separated by an impact parameter vector $\vec{b}$ which we choose to point along the $\hat{x}$ direction, i.e., $\vec{b} = b\hat{x}$. We choose to locate the origin of our coordinate system to lie halfway between the center of the two nuclei such that the overlap density can be written as

$$n_{AB}(x, y, b) = T_A(x + b/2, y) T_B(x - b/2, y). \tag{3.3}$$

Another quantity of interest is the participant density which is given by

$$n_{\text{part}}(x, y, b) = T_A(x + b/2, y)\left\{1 - \left[1 - \frac{\sigma_{NN}\, T_B(x - b/2, y)}{B}\right]^B\right\} + T_B(x - b/2, y)\left\{1 - \left[1 - \frac{\sigma_{NN}\, T_A(x + b/2, y)}{A}\right]^A\right\}. \tag{3.4}$$

For LHC collisions at $\sqrt{s_{NN}} = 2.76$ TeV we use $\sigma_{NN} = 62$ mb and for RHIC collisions at $\sqrt{s_{NN}} = 200$ GeV we use $\sigma_{NN} = 42$ mb. From the participant density we construct our first possible initial condition for the transverse energy density profile at central rapidity

$$\mathcal{E}_0^{\text{part}} = \mathcal{E}_0 \frac{n_{\text{part}}(x, y, b)}{n_{\text{part}}(0, 0, 0)}, \tag{3.5}$$

where $\mathcal{E}_0$ is the central energy density obtained in a central collision between the two nuclei.

As an alternative initial condition for energy density one could use the number of binary collisions which is defined as

$$n_{\text{coll}}(x, y, b) = \sigma_{NN}\, n_{AB}(x, y, b), \tag{3.6}$$

from which we obtain the binary collision energy scaling

$$\mathcal{E}_0^{\text{coll}} = \mathcal{E}_0 \frac{n_{\text{coll}}(x, y, b)}{n_{\text{coll}}(0, 0, 0)} = \mathcal{E}_0 \frac{n_{AB}(x, y, b)}{n_{AB}(0, 0, 0)}. \tag{3.7}$$

IV. NUMERICAL METHODS

We consider both smooth and fluctuating initial conditions using three numerical algorithms. In the following two subsections we describe the implementation of each algorithm. In each case detailed below the code is implemented using the C programming language.

A. Centered differences algorithm

In the first algorithm, which we will refer to as the "centered-differences algorithm," we solve Eqs. (2.63) and (2.64) by, first, analytically solving for the individual proper-time derivatives of the four dynamical variables: ξ, Λ, u_x, and u_y using MATHEMATICA [54]. We then had MATHEMATICA output, in C format, the necessary right-hand sides of the four update equations. We then discretize space on a regular square lattice with lattice spacing, $\Delta x = a$. For the spatial derivatives we use centered differences except on the edges of the lattice where we apply either a left- or right-handed first-order derivative. For the temporal updates we use fourth-order Runge-Kutta (RK4) with a step size of $\Delta t = \epsilon$.

For smooth initial conditions the previous method suffices; however, for fluctuating initial conditions one finds that using centered differences introduces spurious oscillations in regions where there are large gradients. In order to damp these oscillations one could attempt to use a two-dimensional Lax-Friedrichs (LAX) update [55,56]. In practice, this amounts to replacing the current value of a given dynamical variable by a local spatial average over neighboring sites and using this as a stand in for the current value of the variable, e.g.,

$$\xi_{\text{LAX}}(\tau, x, y) = [\xi(\tau, x + a, y) + \xi(\tau, x - a, y) + \xi(\tau, x, y + a) + \xi(\tau, y - a)]/4, \tag{4.1}$$

and now the ξ update for a temporal step of size ϵ becomes schematically

$$\xi(\tau + \epsilon, x, y) = \xi_{\text{LAX}}(\tau, x, y) + \epsilon\, R_\xi(\tau, x, y), \tag{4.2}$$

where R_ξ stands for the (rather complicated) right-hand size of the ξ update equation. However, such a scheme results in too much numerical dissipation. An alternative is to realize that the source of the spurious oscillations is the weak coupling between odd- and even-number lattice sites. The full LAX scheme above maximally couples these interleaving lattices; however, this need not be done. Instead, one can weight the LAX-smoothed values with a weight λ and combine this with the current value of the variable in question, e.g.,

$$\xi_{\text{wLAX}}(\tau, x, y) = \lambda \xi_{\text{LAX}}(\tau, x, y) + (1 - \lambda)\xi(\tau, x, y). \tag{4.3}$$

The smaller the value of λ, the less the numerical viscosity. In practice, we have found that for the aHydro equations one should take $\lambda > 0.02$ in order to achieve numerical stability. In the results section below we use $\lambda = 0.05$ which represents a factor of 20 decrease in the dissipation induced by LAX smoothing. Note that, when activated, wLAX smoothing is implemented for all dynamical variables (Λ, ξ, u_x, and u_y) after each full time step of ϵ and not within each RK4 substep. We will only need to use the wLAX method for fluctuating initial conditions; however, in Appendix B we present numerical tests using it in the smooth initial conditions case in order to show that the amount of numerical viscosity in the wLAX case is not numerically significant. That said, one would also like to have another method for handling the spurious oscillations caused by using higher-order centered differences. This has motivated us to also implement the Kurganov-Tadmor central scheme which we describe in the next subsection.

B. The MUSCL algorithm

As mentioned above, when there are large gradients present in a hyperbolic partial differential equation, the application of straightforward centered-differences scheme can lead to spurious oscillations. For smooth initial conditions and finite shear viscosity this is not an issue; however, for fluctuating initial conditions one needs a way to handle shocks and discontinuities. One way to proceed is to implement the LAX method as described previously; however, the LAX method introduces numerical viscosity into the algorithm which scales like the $(\Delta x)^2/\Delta t$ so it is not possible to take the temporal step size to zero without having extremely small lattice spacing to reduce the numerical viscosity. As discussed above, one can reduce the amount of numerical viscosity by instead using the weighted LAX (wLAX) prescription described above; however, it is desirable to have an alternative algorithm in order to be sure of the results.

For this purpose we have also implemented monotone upstream-centered schemes for conservation laws (MUSCL) derived by Kurganov and Tadmor [57] which has been extended to include nonlinear sources [58]. This method is particularly appealing because it can be shown that, although it does induce some numerical viscosity, the magnitude of the numerical viscosity induced scales like as a power of the lattice spacing with no power of the temporal step size in the denominator, allowing one to take extremely small time steps without inducing large artificial numerical viscosity. Our implementation closely follows that introduced by Schenke *et al.* [59] to solve three-dimensional relativistic ideal hydrodynamics equations. They have also extended the method to second-order three-dimensional relativistic viscous hydrodynamics [20,21] with fluctuating initial conditions.

To explain the algorithm, let us consider the simpler case of a one-dimensional system of hyperbolic partial differential equations which can be cast into "conservative" form, i.e.,

$$\partial_t u + F_x(u) = 0, \tag{4.4}$$

where u is, in general, an n-dimensional vector, F is a so-called flux variable or flux function, and $F_x(u) = \partial_x F(u)$. For example, if one were solving the advection equation $\partial_t u + \partial_x u = 0$, then we would have $F = u$ and if one were solving Burgers' equation $\partial_t u + u\partial_x u = 0$, this can be written in conservative form as $\partial_t u + \partial_x(u^2/2) = 0$ so, in this case, $F = u^2/2$. Given a partial differential equation of the form (4.4) Kurganov and Tadmor derived the following semidiscrete update equation

$$\frac{du_j}{dt} = -\frac{H_{j+1/2}(t) - H_{j-1/2}(t)}{\Delta x}, \tag{4.5}$$

where the numerical flux function H is given by

$$H_{j+1/2}(t) \equiv \frac{F[u^+_{j+1/2}(t)] + F[u^-_{j+1/2}(t)]}{2} - \frac{a^x_{j+1/2}(t)}{2}[u^+_{j+1/2}(t) - u^-_{j+1/2}(t)], \tag{4.6}$$

with $a^x_{j+1/2}(t)$ being the local propagation velocity in the x direction, which is given by the maximum of the left and right half-site extrapolated spectral radius of $\partial F/\partial u$, which is defined as ρ

$$a^x_{j+1/2}(t) \equiv \max\left(\rho\left\{\frac{\partial F}{\partial u}[u^+_{j+1/2}(t)]\right), \ \rho\left(\frac{\partial F}{\partial u}[u^-_{j+1/2}(t)]\right\}\right), \tag{4.7}$$

and, finally, the half-site extrapolated intermediate values $u^{\pm}_{j+1/2}$ are given by

$$\begin{aligned} u^+_{j+1/2} &\equiv u_{j+1}(t) - \frac{\Delta x}{2}(u_x)_{j+1}(t)\,, \\ u^-_{j+1/2} &\equiv u_j(t) + \frac{\Delta x}{2}(u_x)_j(t)\,. \end{aligned} \tag{4.8}$$

For the derivatives, u_x, appearing in Eq. (4.8), one should use a total variation diminishing "flux-limiter" so spurious oscillators are avoided [60]. We follow the original paper of Kurganov and Tadmor and use the three-argument minmod flux-limiter [61],

$$(u_x)_j = \text{minmod}\left(\theta\frac{u_j - u_{j-1}}{\Delta x}, \frac{u_{j+1} - u_{j-1}}{2\Delta x}, \frac{u_{j+1} - u_j}{\Delta x}\right), \quad 1 \leqslant \theta \leqslant 2, \tag{4.9}$$

where

$$\text{minmod}(x_1, x_2, \cdots) = \begin{cases} \min_j\{x_j\}, & \text{if} \quad x_j > 0 \quad \forall\, j \\ \max_j\{x_j\}, & \text{if} \quad x_j < 0 \quad \forall\, j\,. \\ 0 & \text{otherwise} \end{cases} \tag{4.10}$$

The value of θ controls the dissipation of the flux limiter, with $\theta = 1$ being the most dissipative and $\theta = 2$ being the least. In this paper we follow Ref. [59] and use $\theta = 1.1$. For details of the derivation of the Kurganov-Tadmor scheme, we refer the reader to their original paper [57]. As mentioned above one can extend the Kurganov-Tadmor scheme to accommodate nonlinear time-dependent sources. Including the possibility of a time-dependent source changes our one-dimensional example to

$$\partial_t u + F_x(u) = J(t, u), \tag{4.11}$$

where J is a source term. Naidoo and Baboolal [58] demonstrated that, in this case, only a simple modification of adding the source on the right-hand side was necessary,

$$\frac{du_j}{dt} = -\frac{H_{j+1/2}(t) - H_{j-1/2}(t)}{\Delta x} + J(t, u_j). \quad (4.12)$$

We note that, to extend the method described thus far to multiple dimensions, one introduces flux functions for each direction, e.g., F_y and F_z, and includes these in the update rule by defining new numerical flux functions (4.6) and propagation velocities (4.7) accordingly.

1. Applying MUSCL to aHydro

In the case of aHydro, all of the evolution equations stem from conservative systems with sources; therefore, we can apply the general method just described. For this purpose, we need the first and second moments of the Boltzmann equation with the RS form for the one-particle distribution function. The zeroth moment can be written in a conservative form with sources in τ-ς coordinates as follows:

$$\partial_\tau j^\tau + \nabla_\perp \cdot \mathbf{j}^\perp = -\frac{j^\tau}{\tau} + J_0, \quad (4.13)$$

where $j^\mu = n\,u^\mu$ is the particle four-current and

$$J_0 \equiv \Gamma\, n_{\rm iso}(\Lambda)\left[\frac{1}{\sqrt{1+\xi}} - \mathcal{R}^{3/4}(\xi)\right] \quad (4.14)$$

is the zeroth-moment of the right-hand side of the Boltzmann equation in the relaxation time approximation used herein. The remaining three update equations necessary can be obtained from energy-momentum conservation, $\partial_\mu T^{\mu\nu} = 0$, giving

$$\partial_\tau T^{\tau\tau} + \partial_x T^{\tau x} + \partial_y T^{\tau y} = -\frac{1}{\tau}[T^{\tau\tau} + \tau^2 T^{\varsigma\varsigma}], \quad (4.15)$$

$$\partial_\tau T^{\tau x} + \partial_x T^{xx} + \partial_y T^{xy} = -\frac{T^{\tau x}}{\tau}, \quad (4.16)$$

$$\partial_\tau T^{\tau y} + \partial_x T^{xy} + \partial_y T^{yy} = -\frac{T^{\tau y}}{\tau}. \quad (4.17)$$

Once the dynamical variables j^τ, $T^{\tau\tau}$, $T^{\tau x}$, $T^{\tau y}$ are updated via these equations, they can then can be used to construct the remaining components of j^μ and $T^{\mu\nu}$. In our case, it is necessary to solve two simultaneous nonlinear equations for ξ and Λ which will then allow us to determine the rest of the information necessary to proceed with the solution. To see how this works in practice, we first use (2.15) to write the nonvanishing components of $T^{\mu\nu}$ and $j^\mu = n\,u^\mu$ explicitly,

$$T^{\tau\tau} = (\mathcal{E} + \mathcal{P}_\perp)u^0 u^0 - \mathcal{P}_\perp, \quad (4.18a)$$
$$T^{\tau i} = (\mathcal{E} + \mathcal{P}_\perp)u^0 u^i, \quad (4.18b)$$
$$T^{ij} = (\mathcal{E} + \mathcal{P}_\perp)u^i u^j, \quad (4.18c)$$
$$T^{ii} = (\mathcal{E} + \mathcal{P}_\perp)u^i u^i + \mathcal{P}_\perp, \quad (4.18d)$$
$$T^{\varsigma\varsigma} = \mathcal{P}_L/\tau^2, \quad (4.18e)$$
$$j^\tau = n\,u^0, \quad (4.18f)$$
$$j^i = n\,u^i, \quad (4.18g)$$

where $i \in \{x, y\}$. Using these equations and the normalization condition $u_\tau^2 = 1 + u_x^2 + u_y^2$, one finds two nonlinear equations, similar to those obtained in Ref. [59],

$$\mathcal{E}(\Lambda, \xi) = T^{\tau\tau} - \frac{(T^{\tau x})^2 + (T^{\tau y})^2}{T^{\tau\tau} + \mathcal{P}_\perp(\Lambda, \xi)} \quad (4.19)$$

and

$$j^\tau = n(\Lambda, \xi)\left[\frac{T^{\tau\tau} + \mathcal{P}_\perp(\Lambda, \xi)}{\mathcal{E}(\Lambda, \xi) + \mathcal{P}_\perp(\Lambda, \xi)}\right]. \quad (4.20)$$

From these two equations one can numerically solve for Λ and ξ. These values can then be used to determine u^τ and u^i via

$$u^\tau = \frac{j^\tau}{n(\Lambda, \xi)}, \quad (4.21a)$$

$$u^i = \frac{n(\Lambda, \xi)\, T^{\tau i}}{j^\tau\,[\mathcal{E}(\Lambda, \xi) + \mathcal{P}_\perp(\Lambda, \xi)]}. \quad (4.21b)$$

Once determined, these components of the four-velocity together with the values of Λ and ξ can be used to determine all remaining variables in Eq. (4.18).

The only remaining ingredient necessary for the Kurganov-Tadmor algorithm to be implemented fully is to determine the local propagation velocities $a^i_{j+1/2}(t)$. These are obtained by evaluating the eigenvalues of the 4×4 Jacobian of j^τ, $T^{\tau\tau}$, $T^{\tau x}$, $T^{\tau y}$. As was the case in Ref. [59], with some work and a little bit of help from MATHEMATICA, one finds that two of the four eigenvalues are degenerate and equal to u^i/u^τ and the other two are given by

$$\lambda_i^\pm = \frac{A \pm \sqrt{B}}{D} \quad (4.22)$$

with

$$A = u^\tau u^i (1 - v^2), \quad (4.23a)$$
$$B = \left[u_\tau^2 - u_i^2 - \left(u_\tau^2 - u_i^2 - 1\right)v^2\right]v^2, \quad (4.23b)$$
$$D = u_\tau^2 - \left(u_\tau^2 - 1\right)v^2, \quad (4.23c)$$

and

$$v^2 = \frac{\partial \mathcal{P}_\perp}{\partial \mathcal{E}} + \frac{n}{\mathcal{E} + \mathcal{P}_\perp}\frac{\partial \mathcal{P}_\perp}{\partial n}. \quad (4.24)$$

Using an ideal equation of state for which $\mathcal{E}_{\rm iso} = 3\mathcal{P}_{\rm iso}$ one obtains

$$v^2(\xi) = \frac{1}{3}\frac{2\mathcal{R}_\perp(\xi) + 3(1+\xi)\mathcal{R}'_\perp(\xi)}{2\mathcal{R}(\xi) + 3(1+\xi)\mathcal{R}'(\xi)} + \frac{4(1+\xi)}{3\mathcal{R}(\xi) + \mathcal{R}_\perp(\xi)}\frac{\mathcal{R}'(\xi)\mathcal{R}_\perp(\xi) - \mathcal{R}(\xi)\mathcal{R}'_\perp(\xi)}{2\mathcal{R}(\xi) + 3(1+\xi)\mathcal{R}'(\xi)}. \quad (4.25)$$

In this function both terms individually diverge in the limit that $\xi \to 0$; however, these divergences cancel to give a finite result of $\lim_{\xi\to 0} v^2 = 2/5$. It has other limits of $\lim_{\xi\to -1} v^2 = 0$ and $\lim_{\xi\to\infty} v^2 = 1/2$. Using the now-known eigenvalues, one finds that the maximum value of the four eigenvalues is given by

$$\rho = |\max(\lambda_i)| = \frac{|A| + \sqrt{B}}{D}. \quad (4.26)$$

Using the above scheme, one can evolve the aHydro system with fluctuating initial conditions; however, there is a caveat, namely that the linearly interpolated intermediate values of j^τ, $T^{\tau\tau}$, $T^{\tau x}$, and $T^{\tau y}$ determined via (4.8) may not have real-valued solutions for Λ and ξ using Eqs. (4.19) and (4.20). In practice, we find that it is necessary to use extremely fine lattices in order to ameliorate this problem. Alternatively, we have found that instead of extrapolating the four variables j^τ, $T^{\tau\tau}$, $T^{\tau x}$, and $T^{\tau y}$ to the half-sites, one can instead extrapolate the current values of Λ and ξ to the half-sites for use in evaluating the flux functions. In addition, we have found that, in practice, it is necessary to use a "hybrid" algorithm in which the centered-differences scheme described in the previous subsection is used as the initial guess for the nonlinear root finder which solves Eqs. (4.19) and (4.20). This is necessary, in particular, in regions where $\xi \simeq 0$ since in this case Eqs. (4.19) and (4.20) have two solutions which become very close together (one positive and one negative). Without external guidance the root finder oscillates between the two solutions. The predicted value from the centered-differences scheme predicts which solution to use in this case for the nonlinear root finder. We will refer to this method as *hybrid Kurganov-Tadmor*.

V. RESULTS

In this section we present results for the time evolution of the matter generated in heavy-ion collisions at LHC energies using the aHydro evolution equations (2.63) and (2.64). For the results presented here we assume an ideal gas of quarks and gluons with $N_f = 2$ so there are $N_{\rm dof} = 37$ degrees of freedom. For our numerical tests and results, we will concentrate on the spatial and momentum-space ellipticities, ϵ_x,

$$\epsilon_x = \frac{\langle y^2 - x^2\rangle_{\mathcal{E}}}{\langle x^2 + y^2\rangle_{\mathcal{E}}}, \tag{5.1}$$

and ϵ_p is defined in the laboratory frame via

$$\epsilon_p = \frac{\langle T^{xx} - T^{yy}\rangle}{\langle T^{xx} + T^{yy}\rangle}, \tag{5.2}$$

where $\langle x^2\rangle_{\mathcal{E}}$ and $\langle y^2\rangle_{\mathcal{E}}$ are the proper-time-dependent average values of x^2 and y^2 weighted by the energy density

$$\langle x^2\rangle_{\mathcal{E}} \equiv \mathcal{N}\int_{x,y} x^2\mathcal{E}(\tau, x, y), \tag{5.3}$$

and the averages in the momentum-space ellipticity represent unweighted integrals over the transverse directions.

Note that the normalization $\mathcal{N}$ is arbitrary since it cancels in the ratio we are computing. These definitions are the conventional ones from the literature [62] which, unfortunately, are slightly inconsistent since ϵ_x is defined in the local rest frame and ϵ_p in the laboratory frame. It would be more consistent to weight the spatial average by $T^{\tau\tau}$; however, to be consistent with the existing literature, we will use the definition weighted with the energy density in the local rest frame.

We concentrate on the ellipticities since, as we will see, large momentum-space anisotropies are developed during the evolution of the system. Such large momentum-space anisotropies cast doubt on the naive application of Cooper-Frye [63] and linearly corrected Cooper-Frye [64]. We, therefore, postpone the implementation of freeze-out until we can allow for large momentum-space anisotropies and, in the meantime, focus on quantities that are independent of the freeze-out prescription.

A. Smooth initial conditions

We begin by presenting results using smooth initial conditions. For numerical tests of the various algorithms we refer the reader to Appendix B. Therein we show scalings with lattice spacing, box size, and comparisons of the different algorithms employed for both smooth and fluctuating initial conditions.

In order to demonstrate that aHydro reproduces known second-order viscous hydrodynamics results, in Figs. 1 and 2 we compare the results of an aHydro run with results obtained using the latest version of the code of Romatschke and Luzum [12]. In Fig. 1 we assumed $4\pi\eta/\mathcal{S} = 0.1$ and in Fig. 2 we assumed $4\pi\eta/\mathcal{S} = 10$. In both cases, we show the

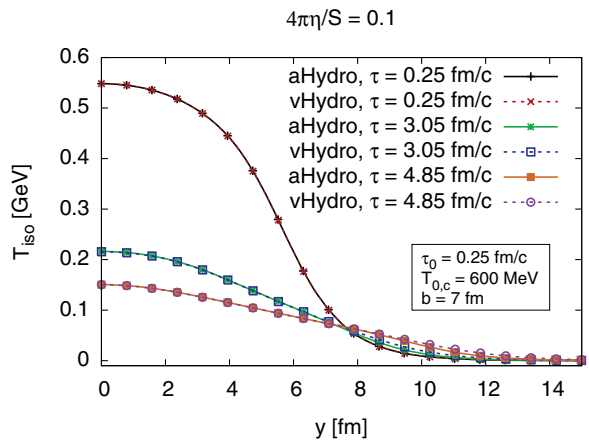

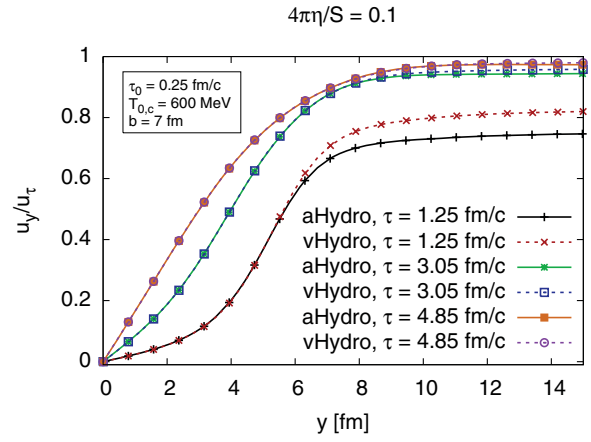

FIG. 1. (Color online) Comparison of aHydro isotropic temperature and flow profiles with second-order viscous hydrodynamics code for $4\pi\eta/\mathcal{S} = 0.1$ and $b = 7$ fm. Lattice size used was 109×109 with $a = 0.394$ fm, $\epsilon = 0.01$ fm/c, $\tau_0 = 0.25$ fm/c, $\Lambda_0 = 600$ MeV, and $\xi_0 = 0$. For the transverse profile Glauber binary collision scaling was used.

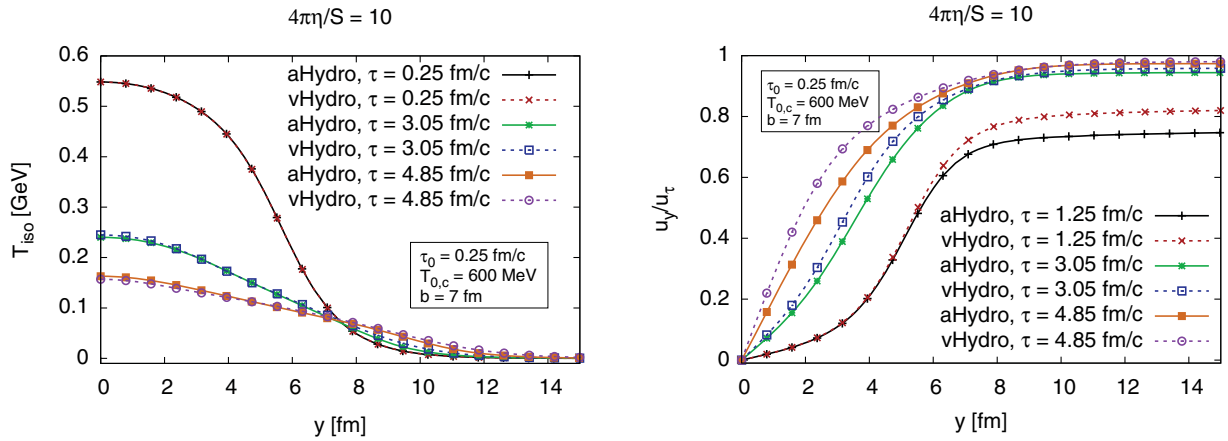

FIG. 2. (Color online) Comparison of aHydro isotropic temperature and flow profiles with second-order viscous hydrodynamics code for $4\pi\eta/\mathcal{S} = 10$ and $b = 7$ fm. Lattice size used was 109×109 with $a = 0.394$ fm, $\epsilon = 0.01$ fm/c, $\tau_0 = 0.25$ fm/c, $\Lambda_0 = 600$ MeV, and $\xi_0 = 0$. For the transverse profile Glauber binary collision scaling was used.

isotropic temperature profile, $T_{\rm iso} = \mathcal{R}^{1/4}(\xi)\mathcal{E}_{\rm iso}(\Lambda)$, in the left panel and the ratio of the y component of the four velocity to the τ component in the right column. As can be seen from Fig. 1 there are only small differences at large radii in the case that the shear viscosity to entropy ratio is small. This demonstrates that our code reproduces second-order viscous hydrodynamics in the limit of small $\eta/\mathcal{S}$. Figure 2 shows the case of large shear viscosity-to-entropy ratio. In this case, we see only small deviations in the temperature profiles and substantial differences in the flow profiles. We therefore expect the aHydro and second-order viscous hydrodynamics frameworks to give different flow observables for large $\eta/\mathcal{S}$. We note that corrections near the edges are expected even for small values of $\eta/\mathcal{S}$ and that the relative magnitude of the aHydro flow and the viscous hydrodynamics flow is to be expected: Since aHydro generates larger longitudinal pressure than viscous hydrodynamics one expects diminished radial flow. This pattern is also observed in simulations which use the lattice-Boltzmann method [65].

In Figs. 3(a) and 3(b) we compare the spatial and transverse momentum-space eccentricities as a function of proper time, assuming two different values of the shear viscosity-to-entropy density ratio corresponding to typical strong-coupling ($4\pi\eta/\mathcal{S} = 1$) and weak-coupling ($4\pi\eta/\mathcal{S} = 10$) values. In Fig. 3(a) we used smooth Glauber wounded-nucleon initial conditions and in Fig. 3(b) we used smooth Glauber binary collision initial conditions. In both figures we assumed $b = 7$ fm, $\Lambda_0 = T_0 = 0.6$ GeV, $\xi_0 = 0$, and $u_{\perp,0} = 0$ at $\tau_0 = 0.25$ fm/c and used the centered-differences algorithm with a lattice size of 100×100, a lattice spacing of $a = 0.4$ fm, and a temporal step size of $\epsilon = 0.01$ fm/c. In both cases, RK4 with a temporal step size of $\epsilon = 0.01$ fm/c was used for the

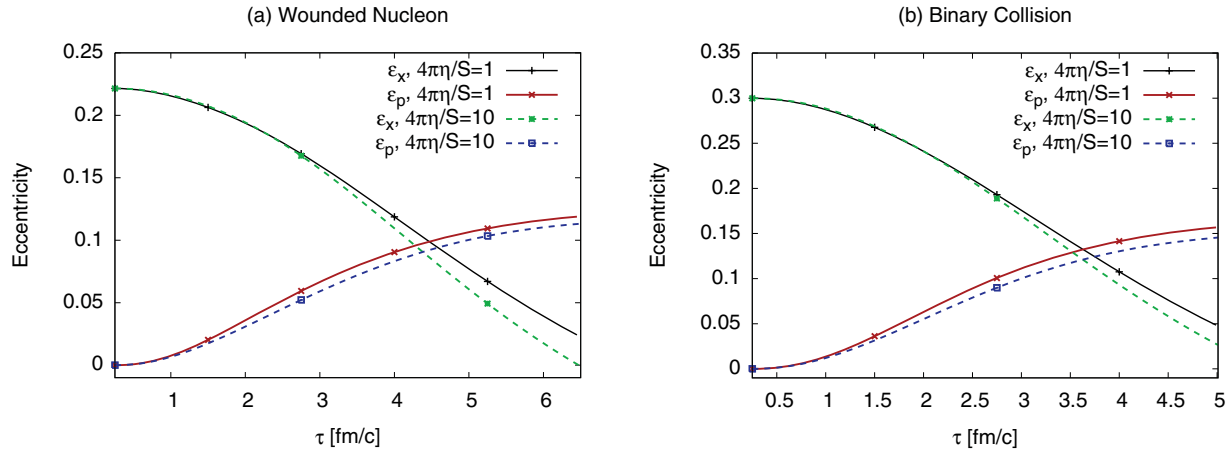

FIG. 3. (Color online) Spatial and momentum eccentricities as a function of proper time for (a) a Glauber wounded-nucleon transverse profile and (b) a Glauber binary-collision transverse profile with $b = 7$ fm, $\Lambda_0 = T_0 = 0.6$ GeV, $\xi_0 = 0$, and $u_{\perp,0} = 0$ at $\tau_0 = 0.25$ fm/c. For the $4\pi\eta/\mathcal{S} = 1$ run we used $\Lambda_0 = T_0 = 0.6$ GeV and for the $4\pi\eta/\mathcal{S} = 10$ run we used $\Lambda_0 = T_0 = 0.576$ GeV for wounded-nucleon initial conditions and $\Lambda_0 = T_0 = 0.584$ for binary-collision initial conditions. These adjustments were made in order to guarantee the same final particle number. In all cases we used the centered-differences algorithm with a lattice size of 100×100, a lattice spacing of $a = 0.4$ fm, and a RK4 temporal step size $\epsilon = 0.01$ fm/c.

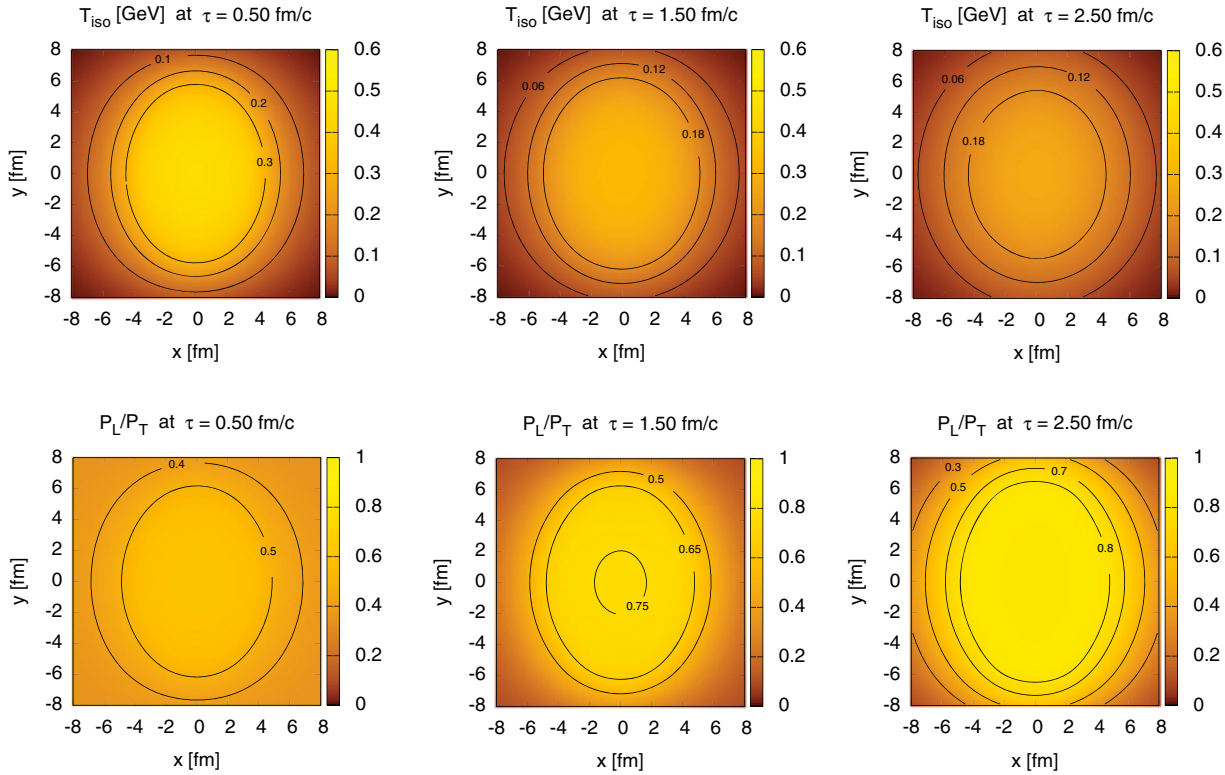

FIG. 4. (Color online) Visualization of the isotropic temperature and pressure anisotropy at three different times after the nuclear impact. For these plots we assumed a noncentral collision with $b = 7$ fm, an isotropic Glauber wounded-nucleon profile, and a $b = 0$ fm central temperature of 0.6 GeV at 0.25 fm/c. For this plot we used a value of $4\pi\eta/\mathcal{S} = 1$ and a lattice size of 200×200 with a lattice spacing of $a = 0.2$ fm and a RK4 temporal step size of $\epsilon = 0.01$ fm/c.

updates. As can be seen from these figures, increasing the shear viscosity-to-entropy ratio by a factor of 10 only decreases the momentum-space eccentricity ϵ_p at 5 fm/c by approximately 10% in both cases shown. We note, however, that the dynamical framework employed here, namely assuming that the local rest frame energy momentum tensor is azimuthally symmetric in momentum-space, may underestimate the full effect of the shear viscosity.

In Figs. 4 and 5 we present visualizations in the form of colormaps with contours of the proper-time dependence of the isotropic temperature and the pressure anisotropy defined by the ratio of the longitudinal and transverse pressures. Figure 4 shows the case of $4\pi\eta/S = 1$ and Fig. 5 shows the case of $4\pi\eta/S = 10$. In both cases we assumed a noncentral collision with $b = 7$ fm, a Glauber wounded-nucleon profile, and a $b = 0$ fm central temperature of $\Lambda_0 = T_0 = 0.6$ GeV at $\tau_0 = 0.25$ fm/c. A lattice size of 200×200 with a lattice spacing of $a = 0.2$ fm and a RK4 temporal step size of $\epsilon = 0.01$ fm/c was used in both cases. As we can see from this figure, the magnitude of the momentum-space anisotropies can be large in the center of the fireball and grows toward the edges. In Fig. 4 we see that, assuming $4\pi\eta/S = 1$ at $\tau = 1.5$ fm/c, the center still has a 25% momentum-space anisotropy and, assuming $4\pi\eta/S = 10$ (Fig. 5), one finds approximately 85% momentum-space anisotropy at $\tau = 1.5$ fm/c. In fact, in the case of $4\pi\eta/S = 10$ the system is highly anisotropic during the entire evolution. For such large shear viscosities the aHydro framework provides a dynamical framework which should be more reliable than the naive application of second-order viscous hydrodynamics.

In Fig. 6 we plot the momentum-space eccentricity, ϵ_p, at the "freeze-out time" τ_f as a function of the assumed impact parameter, b. For this figure we used a Glauber wounded-nucleon transverse profile with $\xi_0 = 0$, and $u_{\perp,0} = 0$ at $\tau_0 = 0.25$ fm/c assuming $4\pi\eta/\mathcal{S} = 1$ and $4\pi\eta/\mathcal{S} = 10$ and a freeze-out temperature of $T_f = 0.15$ GeV. For the $4\pi\eta/\mathcal{S} = 1$ run we used $\Lambda_0 = T_0 = 0.6$ GeV as the central temperature and for the $4\pi\eta/\mathcal{S} = 10$ run we used $\Lambda_0 = T_0 = 0.576$ GeV in order to guarantee the same final particle number. We used the centered-differences algorithm with a lattice size of 200×200, a lattice spacing of $a = 0.2$ fm, and a RK4 temporal step size $\epsilon = 0.01$ fm/c. The freeze-out time τ_f was determined by finding the time at which the maximum isotropic temperature $T_{\rm iso}$ dropped below the freeze-out temperature of $T_f = 0.15$ GeV. This figure shows that changing the assumed value of the shear viscosity-to-entropy ratio from 1 to 10 only makes a difference of 8% in the peak value of the momentum-space ellipticity. We should note, as a caveat which we will emphasize again in the conclusions, that, because we assume that the energy momentum tensor is azimuthally symmetric in the local rest frame, this places us somewhere between a full-blown viscous hydrodynamical calculation and ideal hydrodynamics. Therefore, firm conclusions will have to wait until results with a completely general ellipsoidal energy-momentum tensor are available.

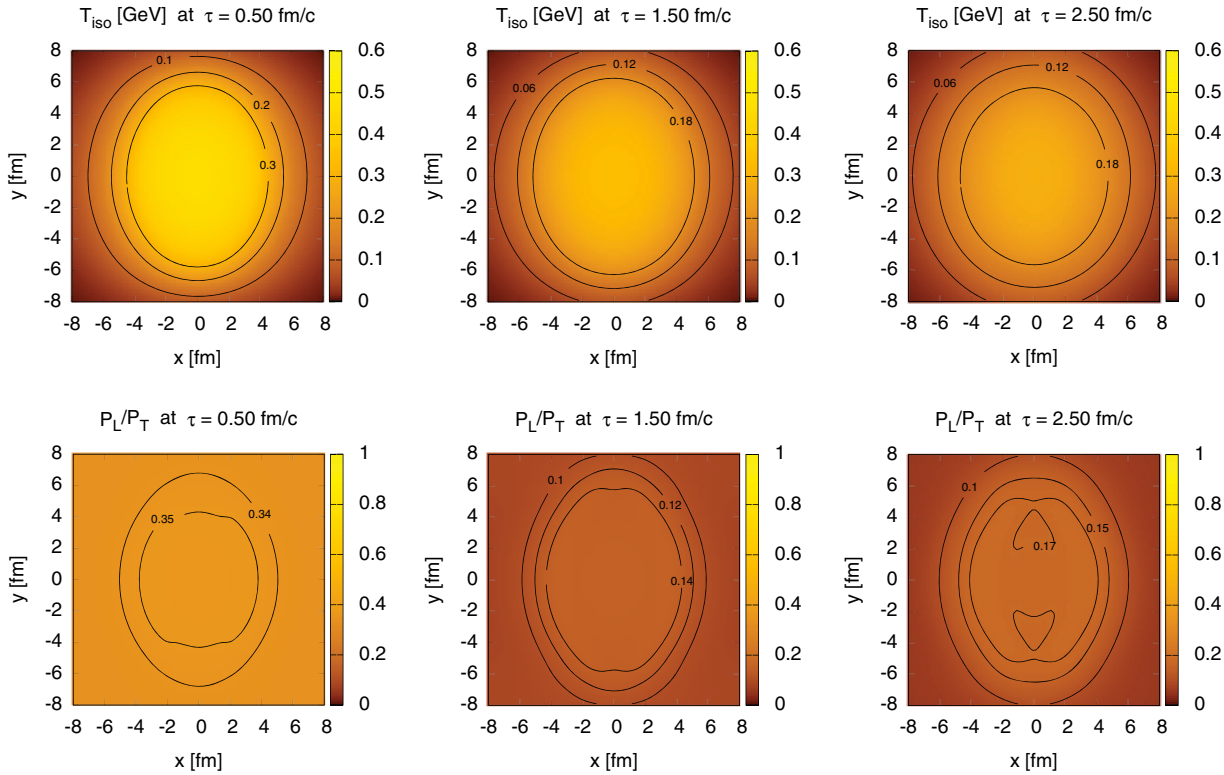

FIG. 5. (Color online) Visualization of the isotropic temperature and pressure anisotropy at three different times after the nuclear impact. For these plots we assumed a noncentral collision with $b = 7$ fm, an isotropic Glauber wounded-nucleon profile, and a $b = 0$ fm central temperature of 0.6 GeV at 0.25 fm/c. For this plot we used a value of $4\pi\eta/\mathcal{S} = 10$ and a lattice size of 200 × 200 with a lattice spacing of $a = 0.2$ fm and a RK4 temporal step size of $\epsilon = 0.01$ fm/c.

B. Fluctuating initial conditions

For our fluctuating initial condition case we have implemented Monte Carlo (MC) Glauber initial conditions [66]. At a given impact parameter b we statistically sample a Woods-Saxon distribution to determine the position of the nucleons in each colliding nuclei. We then compute the transverse distance between each pair of nucleons from nuclei A and B and assume that they collide if the transverse distance between the centers of the nucleons being compared is less than $d \equiv \sqrt{\sigma_{NN}/\pi}$. If a collision is deemed to have occurred a two-dimensional Gaussian with width $\sigma_0 = 0.46$ fm is added to the energy density. We then adjust the overall scale to match the smooth Glauber model results.

In Fig. 7 we present visualizations in the form of color maps with contours of the proper-time dependence of the isotropic temperature and the pressure anisotropy defined by the ratio of the longitudinal and transverse pressures. In Fig. 7 we assumed a central collision $b = 7$ fm with a sampled Monte Carlo Glauber wounded-nucleon profile, an isotropic temperature of $\Lambda_0 = T_0 = 0.6$ GeV at $\tau_0 = 0.25$ fm/c, and $4\pi\eta/\mathcal{S} = 1$. We used a lattice size of 200 × 200 with a lattice spacing of $a = 0.2$ fm and a RK4 temporal step size of $\epsilon = 0.01$ fm/c. As can be seen from this figure, fluctuations can induce large momentum-space anisotropies, particularly in regions where the initial temperature is lower and, therefore, the relaxation rate is smaller. In a second-order viscous hydrodynamical approach one would have many "spots" with very large momentum-space anisotropies. Note that Fig. 7 shows the case $4\pi\eta/\mathcal{S} = 1$ and we do not include a similar

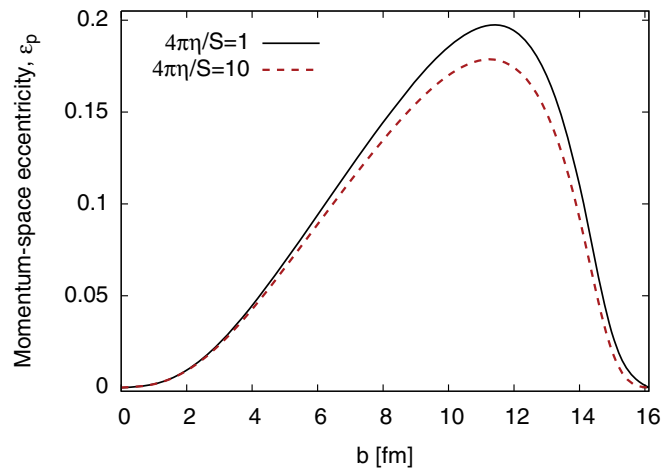

FIG. 6. (Color online) Momentum eccentricity at the freeze-out time as a function of impact for an isotropic Glauber wounded-nucleon transverse profile with $\xi_0 = 0$ and $u_{\perp,0} = 0$ at $\tau_0 = 0.25$ fm/c assuming $T_f = 0.15$ GeV. For the $4\pi\eta/\mathcal{S} = 1$ run we used $\Lambda_0 = T_0 = 0.6$ GeV as the central temperature and for the $4\pi\eta/\mathcal{S} = 10$ run we used $\Lambda_0 = T_0 = 0.576$ GeV in order to guarantee the same final particle number. We used the centered-differences algorithm with a lattice size of 200 × 200, a lattice spacing of $a = 0.2$ fm, and a RK4 temporal step size $\epsilon = 0.01$ fm/c.

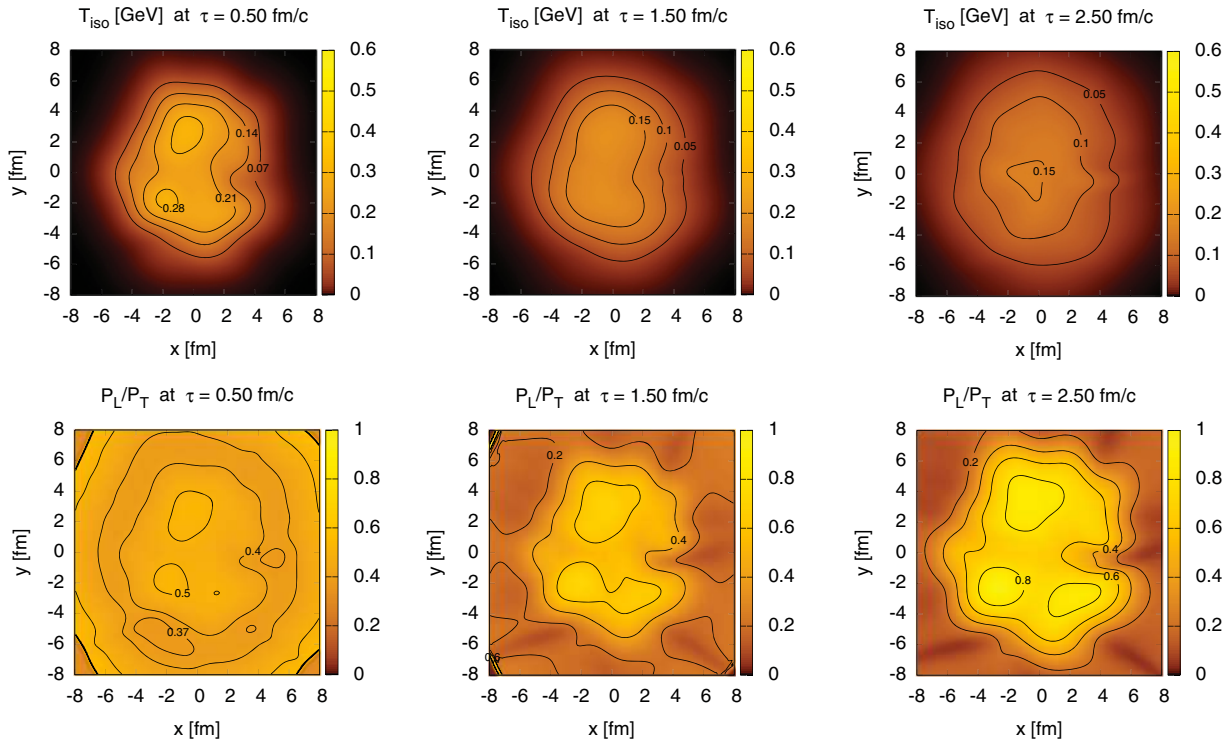

FIG. 7. (Color online) Visualization of the isotropic temperature and pressure anisotropy at three different times after the nuclear impact. For these plots we assumed a collision centrality of $b = 7$ fm with a sampled Monte Carlo Glauber wounded-nucleon profile and an isotropic temperature of $T = 0.6$ GeV at 0.25 fm/c. For this plot we used a value of $4\pi\eta/\mathcal{S} = 1$. We used a lattice size of 200×200 with a lattice spacing of $a = 0.2$ fm and a RK4 temporal step size of $\epsilon = 0.01$ fm/c.

figure for the case of $4\pi\eta/\mathcal{S} = 10$; however, we note that similarly to the case of smooth initial conditions, for this large value of the shear viscosity-to-entropy ratio, one sees large persistent momentum-space anisotropies throughout the simulated region.

VI. CONCLUSIONS

In this paper we studied the application of anisotropic hydrodynamics to the evolution of the matter created in relativistic heavy-ion collisions. We began by specifying a tensor basis for the energy-momentum tensor which was applicable when the system is azimuthally symmetric such that one has energy density, transverse pressure, and longitudinal pressure along the diagonal in the local rest frame. Microscopically we were able to demonstrate that if one assumes local momentum-space azimuthal symmetry, it suffices to introduce one scale Λ and an anisotropy parameter, ξ, which controls the transverse-longitudinal momentum-space anisotropy.

We then used these results in the computation of moments of the Boltzmann equation. Using the zeroth and first moments of the Boltzmann equation, we were able to determine dynamical equations for the plasma scale, Λ, anisotropy parameter, ξ, and the transverse flow components u_x and u_y. In order to solve the resulting partial differential equations we implemented three differencing schemes: centered differences, weighted LAX, and hybrid Kurganov-Tadmor. The first method is suitable for smooth initial conditions, whereas the second two are required when one considers event-by-event simulations. Based on our analysis and benchmarks, we find the weighted LAX scheme to be faster than the hybrid Kurganov-Tadmor scheme with both giving the same results within controllable numerical errors.

We showed through explicit solution of the resulting partial differential equations that the pressure components remain positive definite and that plasma momentum-space anisotropies grow larger as one approaches the transverse edge. In addition, we studied fluctuating initial conditions and demonstrated that fluctuations can result in regions of high momentum-space anisotropy in the center of the simulated matter. As a cross-check we demonstrated that in the limit of small $\eta/\mathcal{S}$ the solution of the aHydro dynamical equations reproduces results from publicly available second-order viscous hydrodynamics codes. For smooth initial conditions we demonstrated that, subject to the assumption of momentum-space azimuthal symmetry in the local rest frame, one sees a relatively small variation of the final laboratory frame momentum-space eccentricity ϵ_p as $\eta/\mathcal{S}$ is increased. Drawing quantitative conclusions from the results contained herein might be premature, however, since the impact of relaxing the assumption of azimuthal isotropy of the energy momentum tensor in the local rest frame is unknown. Removing this assumption will result in what we will term *ellipsoidal* anisotropic hydrodynamics. Work in this direction is currently underway.

We note in closing that there have been a number of authors studying the behavior of anisotropic plasmas in strongly coupled gauge theories [34,36,67–74]. The aHydro framework agrees extremely well with existing first-, second-, and

third-order viscous hydrodynamical results which have been computed analytically for strongly coupled $\mathcal{N} = 4$ supersymmetric Yang-Mills [75]. It would be interesting to see if any of the results contained herein could be used in the context of strongly coupled theories in order to develop useful phenomenological models. One open question first raised in Ref. [74] concerns whether the breaking of rotational symmetry in momentum space requires the introduction of transverse and longitudinal transport coefficients. Mathematically, this would seem to be the case in our formalism if one linearizes fluctuations around an anisotropic background. Such possibilities will be explored in the future. In the meantime, the progress made here opens up the possibility for phenomenological application to heavy-ion observables such as collective flow, photon and dilepton production, quarkonium screening, jet energy loss, etc., in the presence of large momentum-space anisotropies.

ACKNOWLEDGMENTS

We thank Gabriel Denicol, Wojciech Florkowski, Sangjong Jeon, Harri Niemi, and Björn Schenke for useful conversations during the preparation of this work. M.M. and M.S. thank the H. Niewodniczański Institute of Nuclear Physics and the Frankfurt Institute of Advanced Studies, where part of this work was done. M.S. also thanks the Institute for Nuclear Theory at University of Washington for allowing him to participate in the INT program "Gauge Field Dynamics In and Out of Equilibrium," where the final stages of this work were completed. M.S. was supported by NSF Grant No. PHY-1068765 and the Helmholtz International Center for FAIR LOEWE program. M.M. was supported by Ministerio de Ciencia e Innovacion of Spain under project FPA2009-06867-E.

APPENDIX A: PARTICLE PRODUCTION IN THE (0 + 1)-DIMENSIONAL CASE

In this Appendix we discuss the issue of particle production in second-order viscous hydrodynamics versus anisotropic hydrodynamics. To begin, we note that there are two limits in which one expects particle production to go to zero: (a) the limit of ideal hydrodynamics and (b) the free-streaming limit. For small but nonvanishing shear viscosity we expect there to be additional particles associated with dissipation; however, as the shear viscosity-to-entropy ratio increases, we should see a maximum in the particle production since it will eventually have to go to zero in the free-streaming limit. In contrast, second-order viscous hydrodynamics predicts that the excess in particle production is a monotonically increasing function of the assumed value of $\eta/\mathcal{S}$.

In order to demonstrate the difference quantitatively, in Fig. 8 we plot the quantity $\tau/\tau_0\, n/n_0 - 1$ at $\tau = \tau_f$ as a function of $4\pi\eta/\mathcal{S}$. We used a freeze-out temperature of $T_f = 150$ MeV to determine τ_f. This quantity should be zero if there are no particles produced during the evolution. As can be seen from these plots our expectations are confirmed, namely that one sees a maximum in entropy production at large values of $4\pi\eta/\mathcal{S}$ with it returning to zero as $4\pi\eta/\mathcal{S}$ increases above this point. Concentrating on the zoomed plot in Fig. 8 one sees that for $4\pi\eta/\mathcal{S} = 10$ second-order viscous hydrodynamics overestimates the entropy production by approximately 93%. We note that as the initial temperature is lowered, the excess particle production obtained from second-order viscous hydrodynamics becomes larger. This will be important for phenomenology since one of the key constraints on $\eta/\mathcal{S}$ stems from having to reduce the assumed initial temperature in order to compensate for dissipative particle/entropy production.

APPENDIX B: NUMERICAL TESTS

In Fig. 9 we show the time evolution of the spatial and transverse momentum-space eccentricities as a function of proper time for a smooth Glauber wounded-nucleon transverse profile with $b = 7$ fm, $\Lambda_0 = T_0 = 0.6$ GeV, $\xi_0 = 0$, and $u_{\perp,0} = 0$ at $\tau_0 = 0.25$ fm/c assuming $4\pi\eta/\mathcal{S} = 1$. In all three cases we used a RK4 temporal step size of $\epsilon = 0.01$ fm/c.

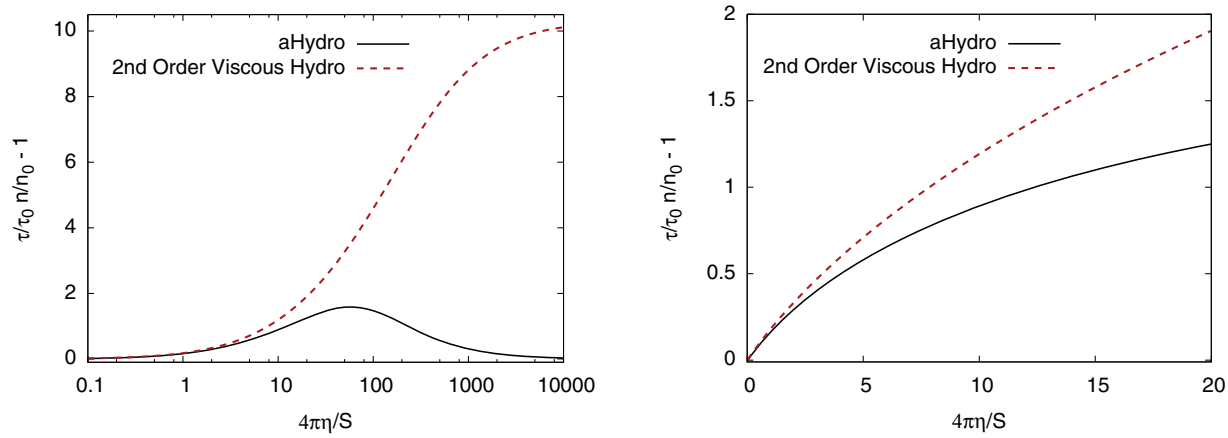

FIG. 8. (Color online) Total particle number at $\tau = \tau_f$ as a function of the assumed value of the shear viscosity-to-entropy ratio. For this figure we ignored transverse expansion, making the system effectively $(0 + 1)$-dimensional, and we used initial values of $\Lambda_0 = 0.6$ GeV and $\xi_0 = 0$ at $\tau_0 = 0.25$ fm/c.

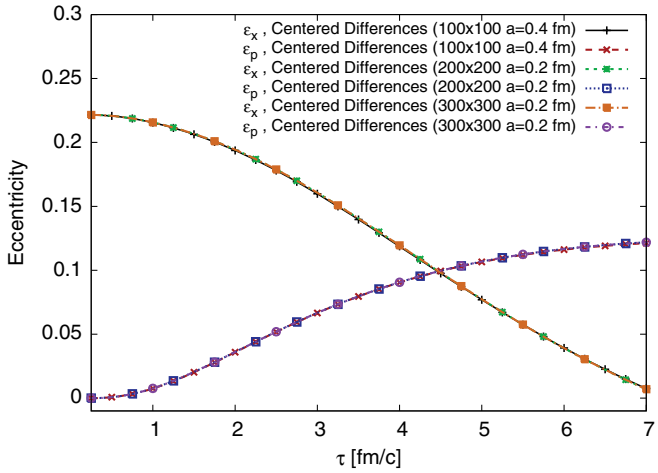

FIG. 9. (Color online) Spatial and momentum eccentricities as a function of proper time for a smooth Glauber wounded-nucleon transverse profile with $b = 7$ fm, $\Lambda_0 = T_0 = 0.6$ GeV, $\xi_0 = 0$, and $u_{\perp,0} = 0$ at $\tau_0 = 0.25$ fm/c assuming $4\pi\eta/\mathcal{S} = 1$. In all three cases we used a RK4 temporal step size of $\epsilon = 0.01$ fm/c.

In this figure we have used the central-differences algorithm without wLAX smoothing and compare the effect of varying the lattice spacing and lattice volume. As can be seen from this figure, the systematics are well under control in this case. Knowing that the centered-differences algorithm systematics are under control, we can now compare with the hybrid Kurganov-Tadmor algorithm. In Fig. 10 we show such a comparison for the same conditions as shown in Fig. 9. As can be seen from this figure, the naive centered-differences algorithm and the hybrid Kurganov-Tadmor algorithm give results that are indistinguishable by eye.

In Fig. 11 we present the spatial and momentum eccentricities as a function of proper time for a smooth Glauber wounded-nucleon transverse profile with $b = 7$ fm, $\Lambda_0 =$

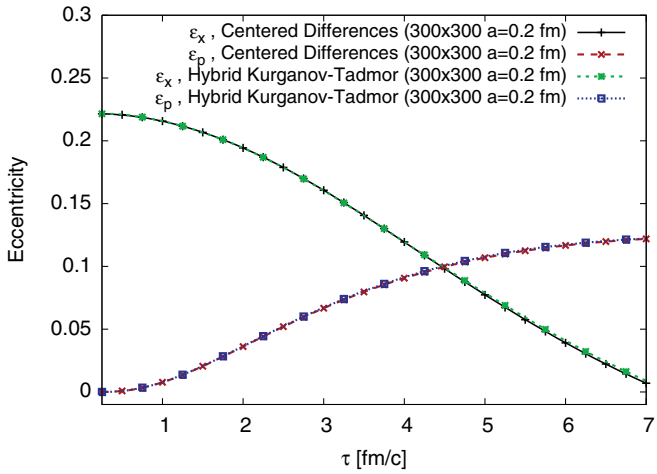

FIG. 10. (Color online) Spatial and momentum eccentricities as a function of proper time for a smooth Glauber wounded-nucleon transverse profile with $b = 7$ fm, $\Lambda_0 = T_0 = 0.6$ GeV, $\xi_0 = 0$, and $u_{\perp,0} = 0$ at $\tau_0 = 0.25$ fm/c assuming $4\pi\eta/\mathcal{S} = 1$. Here we compare the centered-differences and hybrid Kurganov-Tadmor algorithms.

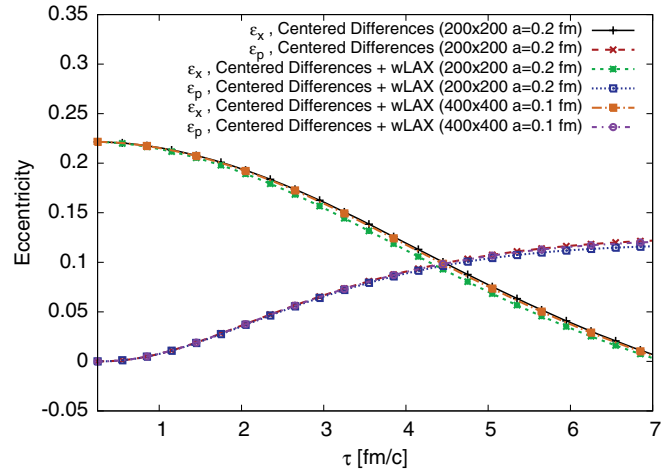

FIG. 11. (Color online) Spatial and momentum eccentricities as a function of proper time for a smooth Glauber wounded-nucleon transverse profile with $b = 7$ fm, $\Lambda_0 = T_0 = 0.6$ GeV, $\xi_0 = 0$, and $u_{\perp,0} = 0$ at $\tau_0 = 0.25$ fm/c assuming $4\pi\eta/\mathcal{S} = 1$. Here we demonstrate the convergence of the wLAX algorithm with $\lambda = 0.05$ to the result obtained without any spatial smoothing as one decreases the lattice spacing. In all cases RK4 with a temporal step size of $\epsilon = 0.01$ fm/c was used.

$T_0 = 0.6$ GeV, $\xi_0 = 0$, and $u_{\perp,0} = 0$ at $\tau_0 = 0.25$ fm/c assuming $4\pi\eta/\mathcal{S} = 1$. In this plot we compare a run with the unsmeared centered-differences algorithm and the wLAX algorithm with two different lattice spacings. As can be seen from this figure, the amount of numerical viscosity is small and can be reduced if one reduces the lattice spacing.

To further illustrate the reliability of the wLAX algorithm in Fig. 12 we compare a single MC Glauber wounded-nucleon run using both the wLAX and hybrid Kurganov-Tadmor algorithms. Both codes were initialized with the same sampled

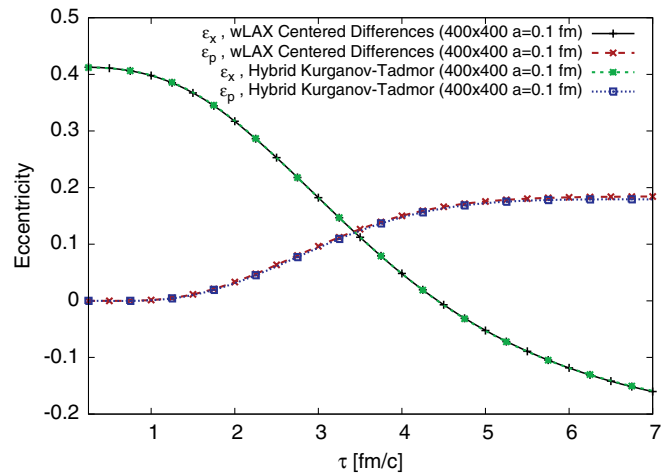

FIG. 12. (Color online) Spatial and momentum eccentricities as a function of proper time for a sampled MC Glauber wounded-nucleon transverse profile with $b = 7$ fm, $\xi_0 = 0$, and $u_{\perp,0} = 0$ at $\tau_0 = 0.25/\text{fm}/c$ assuming $4\pi\eta/\mathcal{S} = 1$. Here we compare the hybrid Kurganov-Tadmor and wLAX algorithms. For the wLAX update we used RK4 with a temporal step size of $\epsilon = 0.01$ fm/c.

MC initial condition (a visualization of the evolution of this configuration is shown in Fig. 7). As can be seen from this figure, wLAX and hybrid Kurganov-Tadmor give virtually indistinguishable results. We point out in this context that the wLAX algorithm take much less time to complete a run giving it a significant advantage when one wants to sample many different configurations. Based on our benchmarks the wLAX algorithm is approximately 10 times faster than the hybrid Kurganov-Tadmor algorithm.

APPENDIX C: BOOST-INVARIANT 1D DYNAMICS—THE BJORKEN SOLUTION

In this section we briefly review what happens when the system is boost invariant and homogeneous in the transverse directions and has conserved particle number, i.e., $J_0 = 0$. For this situation, it is convenient to switch to the comoving Milne coordinates defined as

$$t = \tau \cosh \varsigma, \quad z = \tau \sinh \varsigma. \tag{C1}$$

In this coordinate system the metric $g_{\mu\nu} = \mathrm{diag}\,(1, -1, -1, -\tau^2)$. In addition, the local rest frame four-velocity simplifies to

$$u^\mu = (\cosh \varsigma, 0, 0, \sinh \varsigma), \tag{C2}$$

such that $u_\tau = 1$, $u_\varsigma = 0$, and we have

$$D = u^\mu \partial_\mu = \partial_\tau, \quad \theta = \partial_\mu u^\mu = \frac{1}{\tau}. \tag{C3}$$

By applying the last two expressions to the zeroth moment of the Boltzmann equation (2.26) for an isotropic plasma we obtain

$$\partial_\tau n = -\frac{n}{\tau}, \tag{C4}$$

which has a solution of the form

$$n(\tau) = n_0 \frac{\tau_0}{\tau}. \tag{C5}$$

If now we apply again the expressions given in Eq. (C3) to the first moment of the Boltzmann equation [Eq. (2.32)] one finds easily that

$$\partial_\tau \mathcal{E} + \frac{\mathcal{E} + \mathcal{P}}{\tau} = 0. \tag{C6}$$

If the system has an ideal equation of state (EOS) then $\mathcal{E} = 3\mathcal{P}$ and one can further simplify this to

$$\partial_\tau \mathcal{E} = -\frac{4}{3}\frac{\mathcal{E}}{\tau}, \tag{C7}$$

which has a solution

$$\mathcal{E}_{\text{ideal gas}} = \mathcal{E}_0 \left(\frac{\tau_0}{\tau}\right)^{4/3}. \tag{C8}$$

If the system does not have an ideal EOS but instead has an equation of state corresponding to a constant speed of sound, i.e., $d\mathcal{P}/d\mathcal{E} = c_s^2$, then it follows that $\mathcal{P} = c_s^2 \mathcal{E}$, where we have fixed the constant by demanding that the pressure goes to zero when the energy density goes to zero. In this case one finds instead

$$\mathcal{E} = \mathcal{E}_0 \left(\frac{\tau_0}{\tau}\right)^{1+c_s^2}, \tag{C9}$$

which reduces to the ideal case when $c_s^2 = 1/3$. If the EOS has varying speed of sound then one can express $\mathcal{P}$ in terms of an integral of the speed of sound. Alternatively, one could calculate the pressure and energy density separately for, e.g., an ideal massive Boltzmann gas [76] for which one finds

$$\begin{aligned} \mathcal{E} &= N_{\text{dof}} \frac{e^{\mu/T} m^2 T}{2\pi^2} \left[3T K_2\left(\frac{m}{T}\right) + m K_1\left(\frac{m}{T}\right)\right], \\ \mathcal{P} &= N_{\text{dof}} \frac{e^{\mu/T} m^2 T^2}{2\pi^2} K_2\left(\frac{m}{T}\right), \quad n = \frac{\mathcal{P}}{T}, \end{aligned} \tag{C10}$$

and

$$c_s^2(T, \mu = 0) = \left[3 + \frac{m}{T}\frac{K_2(m/T)}{K_3(m/T)}\right]^{-1}. \tag{C11}$$

Note that the thermodynamic relations above are consistent with Bjorken scaling for the number density, $n/n_0 = \tau_0/\tau$, for all values of m in the case of isotropic hydrodynamics.

[1] P. Huovinen, P. F. Kolb, U. W. Heinz, P. V. Ruuskanen, and S. A. Voloshin, Phys. Lett. B **503**, 58 (2001).
[2] T. Hirano and K. Tsuda, Phys. Rev. C **66**, 054905 (2002).
[3] M. J. Tannenbaum, Rept. Prog. Phys. **69**, 2005 (2006).
[4] P. F. Kolb and U. W. Heinz, *Quark Gluon Plasma*, edited by R. C. Hwa *et al.* (World Scientific, Singapore, 2003), pp. 634-714.
[5] A. Muronga, Phys. Rev. Lett. **88**, 062302 (2002).
[6] A. Muronga, Phys. Rev. C **69**, 034903 (2004).
[7] A. Muronga and D. H. Rischke (2004), arXiv:nucl-th/0407114.
[8] R. Baier, P. Romatschke, and U. A. Wiedemann, Phys. Rev. C **73**, 064903 (2006).
[9] P. Romatschke and U. Romatschke, Phys. Rev. Lett. **99**, 172301 (2007).
[10] R. Baier, P. Romatschke, D. T. Son, A. O. Starinets, and M. A. Stephanov, J. High Energy Phys. 04 (2008) 100.
[11] K. Dusling and D. Teaney, Phys. Rev. C **77**, 034905 (2008).
[12] M. Luzum and P. Romatschke, Phys. Rev. C **78**, 034915 (2008).
[13] H. Song and U. W. Heinz, J. Phys. G **36**, 064033 (2009).
[14] U. W. Heinz, *Relativistic Heavy Ion Physics*, Landolt-Boernstein New Series, edited by R. Stock, Vol. I/23, Chap. 5 (Springer Verlag, New York, 2010).
[15] A. El, Z. Xu, and C. Greiner, Phys. Rev. C **81**, 041901 (2010).
[16] J. Peralta-Ramos and E. Calzetta, Phys. Rev. D **80**, 126002 (2009).
[17] J. Peralta-Ramos and E. Calzetta, Phys. Rev. C **82**, 054905 (2010).
[18] G. Denicol, T. Kodama, and T. Koide, J. Phys. G **37**, 094040 (2010).
[19] G. S. Denicol, T. Koide, and D. H. Rischke, Phys. Rev. Lett. **105**, 162501 (2010).
[20] B. Schenke, S. Jeon, and C. Gale, Phys. Rev. Lett. **106**, 042301 (2011).
[21] B. Schenke, S. Jeon, and C. Gale, Phys. Lett. B **702**, 59 (2011).

[22] P. Bozek, Phys. Lett. B **699**, 283 (2011).
[23] H. Niemi, G. S. Denicol, P. Huovinen, E. Molnar, and D. H. Rischke, Phys. Rev. Lett. **106**, 212302 (2011).
[24] H. Niemi, G. Denicol, P. Huovinen, E. Molnar, and D. Rischke (2012), arXiv:1203.2452.
[25] P. Bozek and I. Wyskiel-Piekarska (2012), arXiv:1203.6513.
[26] G. Denicol, H. Niemi, E. Molnar, and D. Rischke (2012), arXiv:1202.4551.
[27] M. Martinez and M. Strickland, Phys. Rev. C **79**, 044903 (2009).
[28] M. Martinez and M. Strickland, Nucl. Phys. A **856**, 68 (2011).
[29] R. Ryblewski and W. Florkowski, J. Phys. G **38**, 015104 (2011).
[30] M. Strickland and D. Bazow, Nucl. Phys. A **879**, 25 (2012).
[31] M. Strickland, Phys. Rev. Lett. **107**, 132301 (2011).
[32] P. M. Chesler and L. G. Yaffe, Phys. Rev. Lett. **102**, 211601 (2009).
[33] P. M. Chesler and L. G. Yaffe, Phys. Rev. D **82**, 026006 (2010).
[34] M. P. Heller, R. A. Janik, and P. Witaszczyk (2011), arXiv:1103.3452.
[35] M. P. Heller, R. A. Janik, and P. Witaszczyk (2012), arXiv:1203.0755.
[36] M. P. Heller, D. Mateos, W. van der Schee, and D. Trancanelli, Phys. Rev. Lett. **108**, 191601 (2012).
[37] B. Wu and P. Romatschke, Int. J. Mod. Phys. C **22**, 1317 (2011).
[38] P. M. Chesler and D. Teaney (2011), arXiv:1112.6196.
[39] W. Florkowski and R. Ryblewski, Phys. Rev. C **83**, 034907 (2011).
[40] M. Martinez and M. Strickland, Nucl. Phys. A **848**, 183 (2010).
[41] S. R. de Groot, W. A. van Leewen, and C. G. van Weert, *Relativistic Kinetic Theory: Principles and Applications* (Elsevier North-Holland, 1980).
[42] W. Israel and J. M. Stewart, Ann. Phys. **118**, 341 (1979).
[43] A. Muronga, Phys. Rev. C **76**, 014910 (2007).
[44] R. Ryblewski and W. Florkowski, Eur. Phys. J. C **71**, 1761 (2011).
[45] W. Florkowski and R. Ryblewski (2011), arXiv:1111.5997.
[46] W. Israel, Ann. Phys. **100**, 310 (1976).
[47] J. L. Anderson, J. Math. Phys. **15**, 1116 (1974).
[48] R. Ryblewski and W. Florkowski, Acta Phys. Polon. B **42**, 115 (2011).
[49] P. Romatschke and M. Strickland, Phys. Rev. D **68**, 036004 (2003).
[50] P. Romatschke and M. Strickland, Phys. Rev. D **70**, 116006 (2004).
[51] M. Martinez and M. Strickland, Phys. Rev. C **81**, 024906 (2010).
[52] A. Bialas, M. Bleszynski, and W. Czyz, Nucl. Phys. B **111**, 461 (1976).
[53] R. Glauber and G. Matthiae, Nucl. Phys. B **21**, 135 (1970).
[54] Wolfram Research, Inc., MATHEMATICA, *version 7.0*, Champaign, IL (2008).
[55] P. Lax, Commun. Pure Appl. Math. **7**, 159 (1954).
[56] K. Friedrichs, Commun. Pure Appl. Math. **7**, 345 (1954).
[57] A. Kurganov and E. Tadmor, J. Comput. Phys **160**, 241 (2000).
[58] R. Naidoo and S. Baboolal, Future Gener. Comput. Syst. **20**, 465 (2004).
[59] B. Schenke, S. Jeon, and C. Gale, Phys. Rev. C **82**, 014903 (2010).
[60] A. Harten, J. Comput. Phys. **49**, 357 (1983).
[61] B. van Leer, J. Comput. Phys. **14**, 361 (1974).
[62] P. F. Kolb, J. Sollfrank, and U. W. Heinz, Phys. Rev. C **62**, 054909 (2000).
[63] F. Cooper and G. Frye, Phys. Rev. D **10**, 186 (1974).
[64] D. Teaney, Phys. Rev. C **68**, 034913 (2003).
[65] P. Romatschke, M. Mendoza, and S. Succi, Phys. Rev. C **84**, 034903 (2011).
[66] M. L. Miller, K. Reygers, S. J. Sanders, and P. Steinberg, Ann. Rev. Nucl. Part. Sci. **57**, 205 (2007).
[67] R. A. Janik and P. Witaszczyk, J. High Energy Phys. 09 (2008) 026.
[68] D. Mateos and D. Trancanelli, Phys. Rev. Lett. **107**, 101601 (2011).
[69] D. Mateos and D. Trancanelli, J. High Energy Phys. 07 (2011) 054.
[70] M. Chernicoff, D. Fernandez, D. Mateos, and D. Trancanelli (2012), arXiv:1202.3696.
[71] M. Chernicoff, D. Fernandez, D. Mateos, and D. Trancanelli (2012), arXiv:1203.0561.
[72] D. Giataganas (2012), arXiv:1202.4436.
[73] A. Rebhan and D. Steineder, J. High Energy Phys. 08 (2011) 153.
[74] A. Rebhan and D. Steineder, Phys. Rev. Lett. **108**, 021601 (2012).
[75] I. Booth, M. P. Heller, and M. Spalinski, Phys. Rev. D **80**, 126013 (2009).
[76] P. Romatschke, Phys. Rev. D **85**, 065012 (2012).